Cell Reports

Article

pORF3-driven biogenesis of lipid droplets facilitates HEV infectivity

Graphical abstract

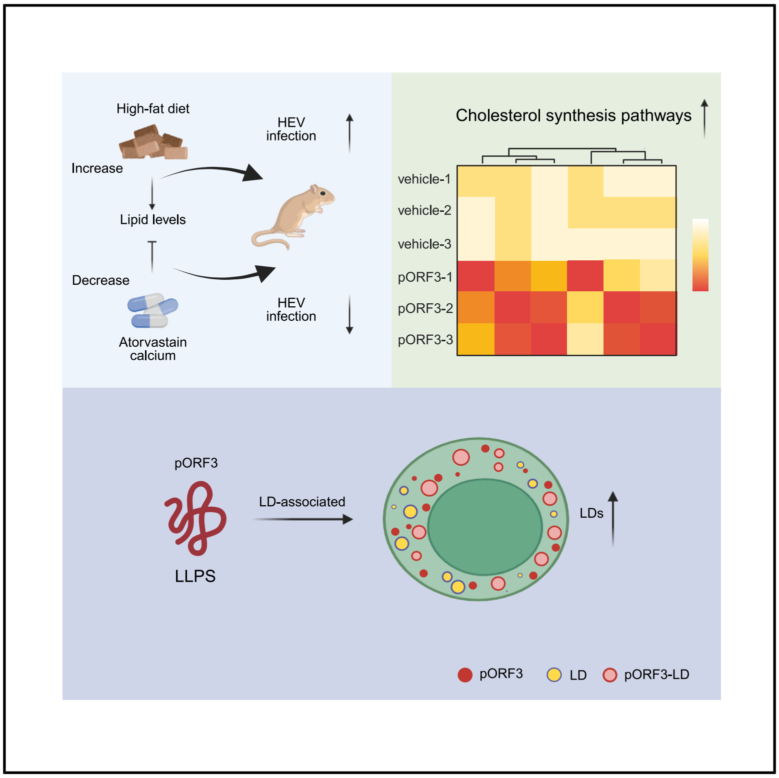

Highlights

- Hepatitis E virus (HEV) infection drives the formation of hepatocyte lipid droplets (LDs)
- pORF3 undergoes LLPS to create a unique LD-associated structure to facilitate LD biogenesis
- pORF3 condensates promote cholesterol/triacylglycerol production for LD anabolism
- Inhibiting LD formation with atorvastatin or deleting ORF3 attenuates HEV infection *in vivo*

Authors

Ling-Dong Xu, Fei Zhang, Can Miao, ..., Cunqi Ye, Yao-Wei Huang, Pinglong Xu

Correspondence

liangtingbo@zju.edu.cn (T.L.),
yecunqi@zju.edu.cn (C.Y.),
yhuang@scau.edu.cn (Y.-W.H.),
xupl@zju.edu.cn (P.X.)

In brief

Xu et al. show that hepatitis E virus hijacks hepatocyte lipid droplets via its small protein pORF3, which phase-separates on droplets, boosts cholesterol synthesis, and expands lipid stores to promote viral replication. By contrast, atorvastatin-driven droplet depletion sharply limits infection in rodents.

Xu et al., 2025, Cell Reports *44*, 116406
October 28, 2025 © 2025 The Authors. Published by Elsevier Inc.
https://doi.org/10.1016/j.celrep.2025.116406

CellPress

Cell Reports

CellPress
OPEN ACCESS

Article

pORF3-driven biogenesis of lipid droplets facilitates HEV infectivity

Ling-Dong Xu,[1,3,4,10] Fei Zhang,[1,2,3,10] Can Miao,[3,10] Xinyuan Yu,[3] Yezhang Zhu,[3] Meng-Di Zhang,[5] Shengduo Liu,[2,3] Siddharth Sridhar,[6] Qiming Sun,[7] Dante Neculai,[7] Qi Zhang,[1,8] Li Shen,[3] Tingbo Liang,[1,8,*] Cunqi Ye,[3,*] Yao-Wei Huang,[5,9,*] and Pinglong Xu[1,2,3,8,11,*]

[1]Department of Hepatobiliary and Pancreatic Surgery and Zhejiang Provincial Key Laboratory of Pancreatic Disease, The First Affiliated Hospital, Zhejiang University School of Medicine, Hangzhou 310058, China
[2]Institute of Intelligent Medicine, ZJU-Hangzhou Global Scientific and Technological Innovation Center, Hangzhou 311215, China
[3]MOE Laboratory of Biosystems Homeostasis & Protection, Zhejiang Provincial Key Laboratory for Cancer Molecular Cell Biology, Life Sciences Institute, Zhejiang University, Hangzhou 310058, China
[4]Laboratory Animal Center, Zhejiang University, Hangzhou 310058, China
[5]Guangdong Laboratory for Lingnan Modern Agriculture, College of Veterinary Medicine, South China Agricultural University, Guangzhou 510642, China
[6]Department of Microbiology, School of Clinical Medicine, Li Ka Shing Faculty of Medicine, The University of Hong Kong, Pokfulam, Hong Kong, China
[7]Department of Cell Biology, Zhejiang University School of Medicine, Hangzhou 310058, China
[8]Cancer Center, Zhejiang University, Hangzhou 310058, China
[9]State Key Laboratory for Animal Disease Control and Prevention, South China Agricultural University, Guangzhou 510642, China
[10]These authors contributed equally
[11]Lead contact
*Correspondence: liangtingbo@zju.edu.cn (T.L.), yecunqi@zju.edu.cn (C.Y.), yhuang@scau.edu.cn (Y.-W.H.), xupl@zju.edu.cn (P.X.)
https://doi.org/10.1016/j.celrep.2025.116406

SUMMARY

Lipid droplets (LDs) are dynamic organelles that mediate lipid metabolism and various cellular processes. However, the interplay between hepatocyte LDs and hepatitis E remains poorly understood. Using targeted lipidomics and lipid profiling in rodent models, we reveal that hepatitis E virus (HEV) infection substantially increases hepatic LD biogenesis. Mechanistically, HEV pORF3 is a key LD biogenesis inducer and an essential factor for viral infectivity *in vivo*. pORF3 undergoes liquid-liquid phase-separation to form condensates that associate with LD phospholipid monolayer peripherally to upregulate cholesterol anabolic pathways, thereby promoting triacylglycerol and cholesterol ester synthesis. Consistently, genetic loss of ORF3 or pharmacologic reduction of LD biogenesis with the statin atorvastatin substantially suppressed HEV infection *in vivo*. These findings identify LD biogenesis as a host dependency for HEV infectivity and propose alternative strategies for HEV intervention by targeting LD-directed metabolic pathways.

INTRODUCTION

Hepatitis E virus (HEV) is a zoonotic pathogen that poses a significant threat to human health, causing both acute and chronic hepatitis.[1,2] Despite its impact, the HEV life cycle remains poorly understood due to limitations in cellular and animal models.[3] HEV possesses a single-stranded, positive-sense RNA genome of around 7.2 kb that consists of a 5′ untranslated region (5′ UTR), three open reading frames (ORF1–ORF3), and a 3′ UTR with a poly(A) tail.[4] ORF1 encodes the nonstructural replicase,[5] ORF2 encodes the capsid protein (with a secreted form known as ORF2S[6]), and ORF3 produces a small multifunctional accessory protein (pORF3). The processing of viral replicase pORF1 remains incompletely understood.[7] We recently reported that processing pORF1 by the host proteasome produces a viral protein HDSA that facilitates the fibrogenic transforming growth factor β (TGF-β)/Small Mothers Against Decapentaplegic (SMAD) pathway.[8] HEV has two forms: nonenveloped virions shed into feces and a membrane-associated, quasi-enveloped form (eHEV) circulating in the blood.[9] Recent research indicates that pORF3, identified as an ion channel protein involved in viral release,[10] also participates in HEV pathogenicity in animal models.[11] pORF3 also facilitates the formation of eHEV by undergoing palmitoylation, which enables its secretion, interaction with Annexin II, and transport into multivesicular bodies for viral egress.[12–14] This discrepancy highlights the need to investigate further how pORF3 orchestrates host cellular physiologies to influence viral replication and disease progression.

Lipid droplets (LDs) are dynamic organelles crucial for cellular energy metabolism,[15,16] bounded by a single phospholipid monolayer that presents an extensive surface area for recruiting enzymes involved in neutral-lipid metabolism.[17] These specialized structures store neutral lipids like Triacylglycerols (TAGs) and cholesterol esters (CEs) and function as reservoirs for

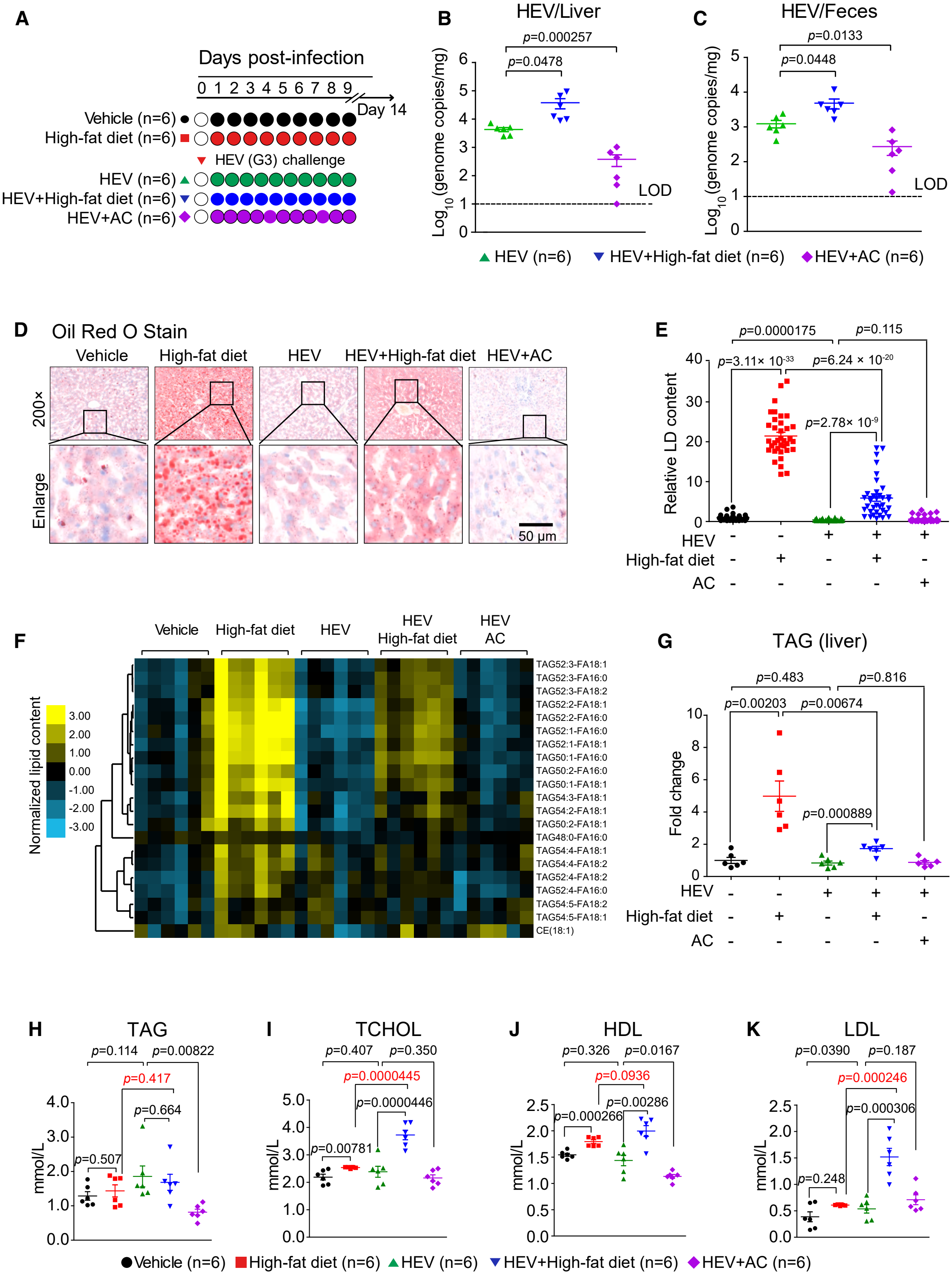

Figure 1. LD levels in gerbil livers are critical for *in vivo* HEV infectivity

(A) The schematic diagram illustrates the experimental groups of HEV-infected gerbils fed high-fat diets and those administered lipid-lowering drugs. The gerbil got infected with HEV upon being inoculated intraperitoneally with 1 mL (1.67 × 10^6 GE/mL).

(legend continued on next page)

membrane synthesis and energy production. Because LDs present a phospholipid monolayer to the cytosol, proteins may form surface-bound condensates that tether to this interface. LDs share compositional similarities with organelle membranes,[18,19] facilitating efficient lipid exchange between LDs and other organelles, such as the endoplasmic reticulum, ensuring membrane homeostasis.[15] Consequently, disruptions in LD metabolism or organelle membrane integrity can contribute to various human diseases.[20,21] LDs have been implicated in the life cycles of some viruses, including hepatitis C virus (HCV),[22,23] dengue virus (DENV),[24] and poliovirus (PV).[25] Nevertheless, the role of LDs and lipid metabolism in the HEV life cycle is incompletely understood.

In this report, we revealed that HEV infection increases LDs in hepatocytes and that high-fat diets promote HEV replication in gerbils while lipid-lowering drugs inhibit it. Our findings indicate that the viral protein pORF3 increases LDs by upregulating the expression of genes involved in cholesterol synthesis through its liquid-liquid phase separation (LLPS) capacity. Through LD biogenesis, pORF3 is essential for viral infectivity *in vivo*. These observations illuminate the intricate relationship between HEV and lipid metabolism, offering potential therapeutic targets.

RESULTS

LD levels in gerbil livers are critical for *in vivo* HEV infectivity

To investigate the role of LDs in HEV infection *in vivo*, we utilized a high-fat diet and atorvastatin calcium (AC) to modulate LD formation in gerbils, serving as a rodent infection model for extensive HEV studies.[26] Triacylglycerols (TAGs) and CEs are key components of LDs.[15] AC potently inhibits high-mobility group-coenzyme A (HMG-CoA) reductase, blocking the mevalonate pathway and lowering intracellular cholesterol levels.[27] Because cholesterol esters make up 15%–30% of LD neutral lipids,[15] their depletion limits LD expansion and secondarily restricts triacylglycerol storage. Moreover, reduced cholesterol feedback on Sterol Regulatory Element-Binding Protein (SREBP)-1c signaling downregulates fatty-acid and TAG biosynthetic enzymes,[28] further contributing to lower TAG availability. Gerbils were randomly assigned to five groups, challenged with genotype 3 (G3) HEV, and treated with vehicle, high-fat diet, or AC (20 mg/kg, three times daily) (Figure 1A). Besides, histological examination using hematoxylin and eosin (H&E) staining revealed the reduced pathological damage in the gerbil livers upon AC treatment, compared to those infected with HEV alone (Figures S1A and S1B). qPCR analysis revealed that HEV RNA copies in the liver of the high-fat diet group were significantly higher; in contrast, those in the AC-treated group were significantly lower (Figure 1B). Similar patterns were observed of HEV RNA copies in the feces (Figure 1C). Noticeably, HEV infection led to substantial consumption of LDs in the gerbil livers, while the high-fat diet group infected with HEV showed a decrease in LDs compared to the high-fat diet group without infection (Figures 1D and 1E). Similarly, the HEV group showed a decrease in the LDs compared to the vehicle group (Figure S1C). Principal component analysis (PCA) revealed the substantial separation in lipid profiles among the five gerbil groups (Figure S1D). An analysis of liver homogenate indicated significant decreases in TAG in the HEV high-fat diet group compared to the high-fat diet only group (Figure S1E). The heatmap of these neutral lipid species also supported this observation, demonstrating that HEV infection reduced TAG in the liver (Figure 1F). Specifically, the HEV high-fat diet group exhibited significantly lower TAG levels compared to the high-fat diet only group (Figure 1G). These observations suggest a positive correlation between liver LD levels and HEV titer *in vivo*, indicating an LD-related HEV infectivity. Intriguingly, total cholesterol and LDL levels in serum were significantly higher in HEV-infected gerbils than in corresponding controls (Figures 1H–1K), indicating that HEV infection drives lipid mobilization into the bloodstream, potentially as a consequence of pORF3-mediated virion envelopment and release.[10,11,26,29] The exact significance of this lipid transfer is unclear, though it probably reduces LD levels in hepatocytes (Figures 1D and 1E) and thus requires a mechanism to sustain these LDs in hepatocytes.

Lowering LD levels compromises HEV replication in hepatic cells

We employed a strategy to reduce LD biogenesis to investigate the impact of LD levels on *in vitro* HEV replication. Huh7-S10-3 cells treated with AC (10 μM) for 48 h were subjected to Lipidtox staining and quantitative image analysis. Fluorescence microscopy revealed that the AC group exhibited significantly lower relative fluorescence intensity than the mock group (Figures 2A and 2B). The AC group demonstrates fewer LDs and smaller relative LD diameters compared to the mock group (Figures 2C and 2D). Next, we investigated the role of LDs in HEV in a persistent HEV replicon system, which can replicate viral RNA but cannot package the viral genome or produce infectious particles due to the deficiency of pORF2 and pORF3.[30] AC was applied in this HEV replicon system, and NVP-HSP990, an HSP90 inhibitor, served as a positive control for inhibiting HEV replication.[31] AC significantly inhibited HEV replicon RNA titers in the HEV replicon

(B and C) Quantitative RT-PCR analysis revealed a significant increase in HEV RNA copy number in the livers and feces of gerbils fed the high-fat diet. Treatment with the cholesterol inhibitor AC (20 mg/kg, 3 times daily) showed a notable decrease in HEV RNA levels. Data were analyzed using a one-way ANOVA test with Bonferroni correction.

(D and E) Oil red O staining confirmed the levels of hepatic LDs in the HEV-infected gerbils with a high-fat or standard diet (6 microscopic fields from each gerbil were randomly selected for statistical analysis). Data were analyzed using a one-way ANOVA test with Bonferroni correction. Scale bars, 50 μm.

(F) Heatmaps of lipid metabolism visually highlighted the lipid anabolic differences among the five gerbil groups. For heatmap generation, clustering analysis was performed on the top 20 most abundant TAG species (ranked by lipidomic abundance) and the detected CE species.

(G) Targeted lipid mass spectrometry-based statistical analysis demonstrated variations in the relative TAG levels among the five gerbil groups. Data were analyzed using a one-way ANOVA test with Bonferroni correction.

(H–K) Serum analyses of lipid profiles displayed elevated TAG, TCHOL, HDL, and LDL levels in the group receiving both the high-fat diet and HEV infection compared to those receiving either treatment alone. Data were analyzed using a one-way ANOVA test with Bonferroni correction.

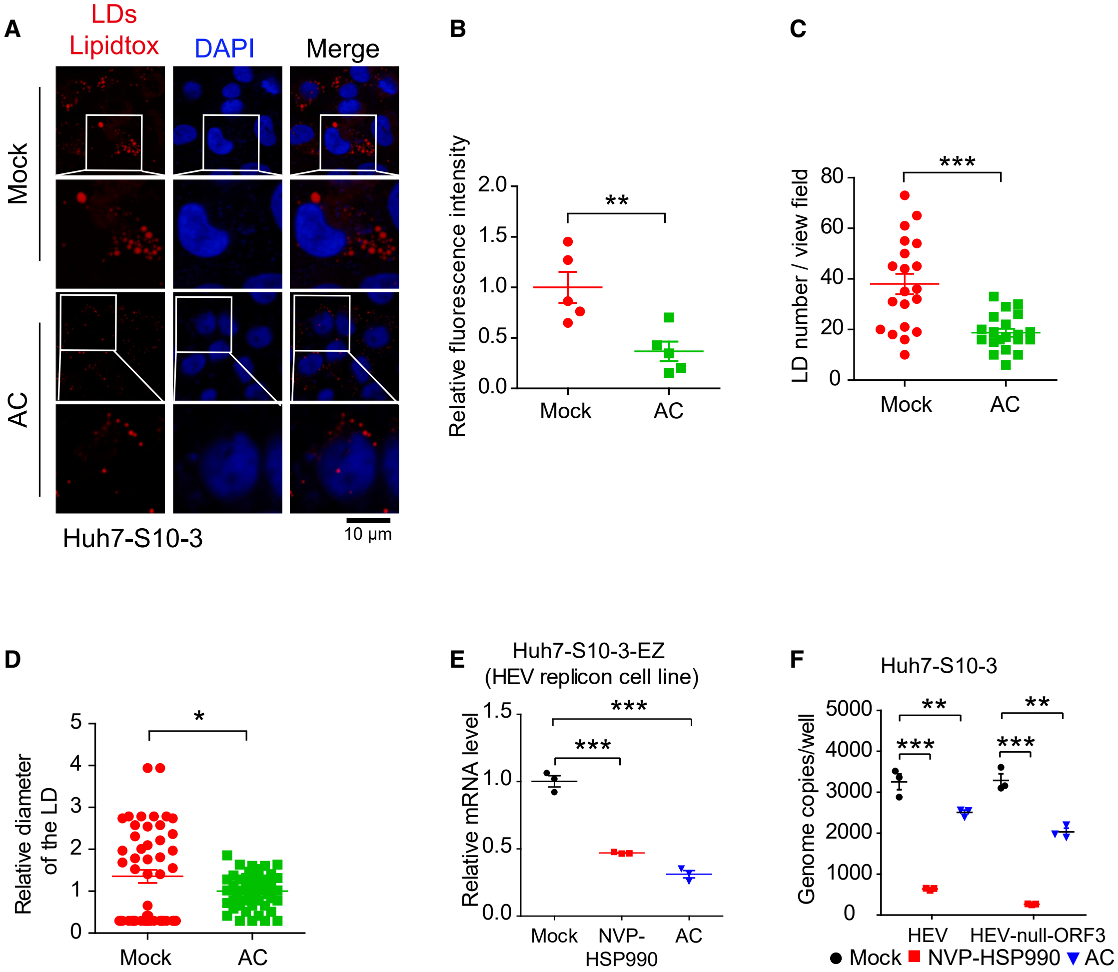

Figure 2. Lowering LD levels compromises HEV replication in hepatic cells

(A and B) AC (10 μM, 48 h) treatment reduces LD content in cells. Left: representative Lipidtox-stained LDs (green) and DAPI (blue). Right: quantification of relative fluorescence intensity. Scale bars, 10 μm. Data were analyzed using a one-way ANOVA test with Bonferroni correction. $^{**}p < 0.01$.

(C and D) AC treatment (10 μM, 48 h) decreases the number and diameter of LDs compared to the mock group. Data were analyzed using a one-way ANOVA test with Bonferroni correction. $^{*}p < 0.05$, $^{***}p < 0.001$.

(E) AC suppresses HEV RNA titers in a replicon system (lacking pORF2/pORF3). NVP-HSP990 (HSP90 inhibitor) serves as a positive control. Data were analyzed using a one-way ANOVA test with Bonferroni correction. $^{***}p < 0.001$.

(F) AC inhibits HEV RNA levels in Huh7-S10-3 cells with persistent HEV-WT or HEV-null-ORF3 infection. Data were analyzed using a one-way ANOVA test with Bonferroni correction. $^{**}p < 0.01$, $^{***}p < 0.001$.

cell line (Figure 2E), consistent with the reduction in HEV RNA levels observed *in vivo*. Huh7-S10-3 cells with persistent HEV infection were additionally examined. AC significantly inhibited HEV RNA titers in the persistent HEV infection cell systems (Figure 2F). These observations suggest a critical role of intracellular levels of LDS in HEV replication.

HEV infection triggers a pORF3-dependent increase of LDs

To assess the impact of HEV infection on LDs and the potential role of pORF3, we employed an HEV RNA infection system that included wild-type HEV (HEV-WT) and HEV-null-ORF3 variants. HEV-null-ORF3 was constructed by using the reverse genetics system, by which we introduced a mutation into the third ATG codon within the subgenomic region encoding the pORF3 protein, which effectively silenced the expression of HEV pORF3 without affecting viral replication and infection, as previously reported.[26,32] Specifically, viral RNA was synthesized via *in vitro* transcription, and upon transfection into Huh7-S10-3 cells, HEV RNA was propagated through serial passages, establishing a persistently infected cell line (Figure S2A, a and b).[33] Quantitative reverse-transcription PCR (RT-qPCR) analysis confirmed that the replication efficiencies of HEV-WT and HEV-null-ORF3 were comparable (Figure S2B), indicating that the absence of pORF3 did not significantly impair HEV replication in the *in vitro* Huh7-S10-3, consistent with prior research.[34] Intriguingly, using BODIPY 493/503 to detect LDs or LiveDrop-mCherry markers for labeling nascent LDs,[35] fluorescence

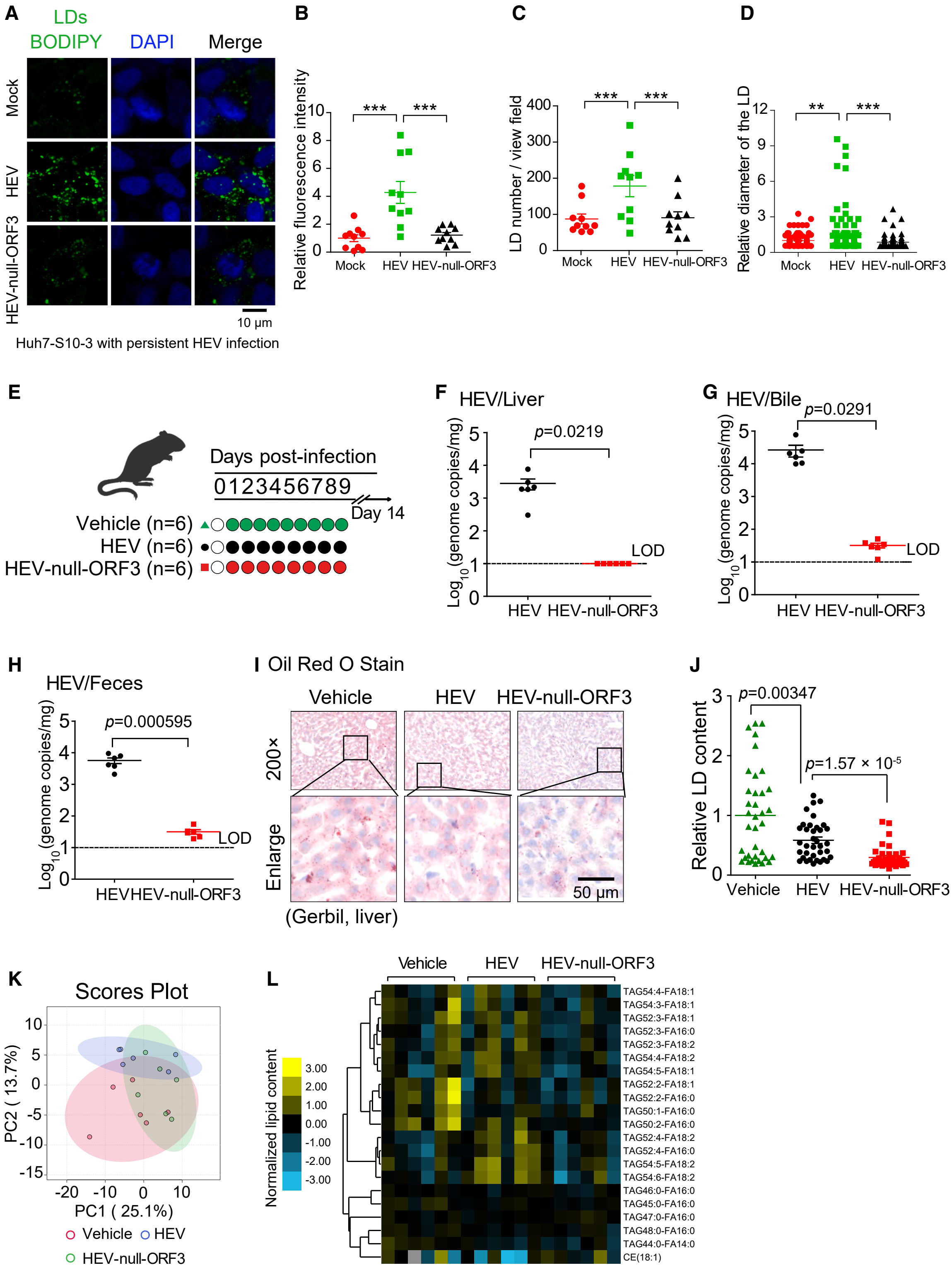

Figure 3. HEV infection triggers a pORF3-dependent increase of LDs

(A) HEV or HEV-null-ORF3 capped RNA transcripts were prepared from the HEV infectious cDNA clone using the mMESSAGE mMACHINE T7 ULTRA transcription kit (Ambion). Then, two HEV-capped RNA transcripts were transfected into Huh7-S10-3 cells and continuously cultured to prepare a cell culture system for sustained HEV infection as described.[33] Huh7-S10-3 with persistent HEV wild-type HEV (HEV-WT) infection leads to a marked enhancement of LDs compared

(legend continued on next page)

microscopy revealed that the HEV-WT group exhibited significantly higher relative fluorescence intensity than the mock and HEV-null-ORF3 groups (Figures 3A, 3B, S2C, and S2D). HEV-WT infection resulted in a substantially increased number of LDs and an increased LD diameter (Figures 3C, 3D, S2E, and S2F), suggesting a potential role of pORF3 in promoting LD biogenesis.

Next, we utilized an HEV gerbil infection model to investigate the effects of HEV infection on LD formation in the livers, employing the same HEV RNA infection system, including HEV-WT and HEV-null-ORF3. Notably, viral titers in the gerbil liver, bile, and feces were significantly lower in HEV-null-ORF3-infected animals compared to those infected with HEV-WT (Figures 3E–3H), reminiscent of previous observations in HEV infection of macaques and liver-humanized mice.[11,36] Noticeably, RNA levels of HEV-null-ORF3 in the livers fell below the detection threshold (Figure 3F), suggesting that the absence of pORF3 severely impaired HEV replication. Histological examination using H&E staining showed reduced liver inflammation in the HEV-null-ORF3 group compared to the HEV-WT group (Figures S2G and S2H), as expected. Intriguingly, an oil red O staining revealed that the HEV-WT group exhibited a higher LD content than the HEV-null-ORF3 group in gerbil livers, though both infections resulted in a significant decrease in liver LDs (Figures 3I and 3J). To examine the effect of HEV-WT or HEV-null-ORF3 infection on lipid metabolism, we analyzed infected gerbil livers by targeted lipid mass spectrometry. A lipid profile separation was evident between the HEV-WT group and the HEV-null-ORF3 group (Figure 3K). Specifically, the heatmap of neutral lipid species revealed that the HEV-null-ORF3 group exhibited lower TAG levels compared to the vehicle or HEV group, suggesting a role of pORF3 in elevating liver TAG during HEV infection (Figure 3L). These observations *in vitro* and in gerbils suggest that HEV infection induces a pORF3-dependent LD anabolism. However, limitations of the *in vitro* system may obscure the precise role of pORF3 in HEV infection *in vivo*.

pORF3 associates with LDs and induces LD biogenesis *in vitro* and gerbil livers

Given the possible involvement of pORF3 in LD metabolism and the critical role of LDs in HEV replication during authentic HEV infection, we investigate the effect and mechanisms of pORF3 in LD biogenesis in two distinct experimental systems: a stably expressing system of pORF3 (HeLa-pORF3-GFP) and the recombinant adenovirus-mediated pORF3 expression in Huh7-S10-3 (Ad5-pORF3). HeLa-pORF3-GFP stable cell lines with HEV G1, G3, and G4 pORF3 expression were generated, and their subcellular localization was analyzed. Noticeably, an evident pORF3 puncta and their precise colocalization with LDs were found (Figure S3A), and over 80% of pORF3 puncta overlapped with LDs, including pORF3 from all three HEV genotypes (Figure S3B). Intriguingly, immunofluorescence analyses employing LiveDrop-mCherry revealed that either fluorescence intensity, number, or size LDs were substantially enhanced in pORF3-expressing cells compared to GFP control (Figures S3C–S3E). Employing a well-defined LD membrane protein perilipin 2 (PLIN2) as a marker, both the high-resolution microscopy and confocal microscope confirmed that pORF3 is associated with LDs (Figures 4A and 4B). We additionally labeled LDs with BODIPY 493/503, which similarly detected the colocalization between LDs and pORF3 (Figure S3F). Noticeably, pORF3 proteins were visualized by immunoblotting of LD samples isolated from Huh7-S10-3 cells with persistent HEV infection (Figure S3G), suggesting an evident pORF3-LD association. Ad5-pORF3 infection in Huh7-S10-3 cells similarly observed substantially higher LD numbers and size in the pORF3 group compared to GFP control (Figures 4C–4F), and intriguingly, electron microscopy confirmed the observation for pORF3-increased LDs with similar unique structure architecture (Figure 4G). These findings indicate a significant role of pORF3 in inducing LD formation and a rarely seen LD architecture containing viral pORF3.

To gauge the capability of pORF3 to stimulate LD formation *in vivo*, we infected Ad5-pORF3 in gerbils, with Ad5-GFP as the negative control (Figure 4H). Notably, Oil Red O staining revealed a significant increase in LDs, both in number and size, in livers from Ad5-pORF3-infected gerbils (Figures 4I and 4J). These *in vitro* and *in vivo* observations indicate an unexpected function of pORF3 in promoting LD formation, which is critical in HEV infectious life cycles.

pORF3 forms liquid-liquid phase separation to facilitate lipid anabolism

LLPS is a molecular and cellular process with pivotal and multifaceted biological roles.[37] Since we have observed pORF3 puncta (Figure S4A), we established and analyzed stable HeLa cells expressing three distinct genotypes of pORF3-GFP fusion proteins to investigate whether pORF3 exhibits LLPS properties. Polymerization of pORF3, which correlated positively with the transfection doses, was evident in

---

to infection with an HEV mutant lacking the ORF3 gene (HEV-null ORF3). LDs were visualized using the BODIPY 493/503 in Huh7-S10-3 cells with persistent HEV infection. Scale bars, 10 μm.

(B–D) Statistical analysis revealed that HEV-WT significantly increased LD numbers, their relative fluorescence intensity, and LD diameter compared to HEV-null ORF3. Data were analyzed using a one-way ANOVA test with Bonferroni correction. $^{**}p < 0.01$, $^{***}p < 0.001$.

(E) The schematic diagram illustrates the gerbil infection model.

(F–H) The gerbils got infected with HEV or HEV-null-ORF3 upon being inoculated intraperitoneally with 1 mL (1.67×10^6 GE/mL). Viral titers were measured in the liver, bile, and feces to compare WT and HEV-null ORF3 viruses. Data were analyzed using a one-way ANOVA test with Bonferroni correction.

(I and J) Oil red O staining of liver sections reveals an increased abundance of LDs in gerbils infected with wild-type HEV compared to those infected with HEV-null ORF3 (I) and calculated by statistical analysis (J) (six microscopic fields from each gerbil were randomly selected for statistical analysis). Data were analyzed using a one-way ANOVA test with Bonferroni correction.

(K) PCA of lipid profiles separates the HEV-WT and HEV-null-pORF3 groups, indicating distinct lipid metabolic patterns influenced by HEV infection.

(L) Heatmaps of lipid metabolism visually highlighted the lipid anabolic differences among the vehicle, HEV-WT, and HEV-null-pORF3 groups. For heatmap generation, clustering analysis was performed on the top 20 most abundant TAG species (ranked by lipidomic abundance) and the detected CE species.

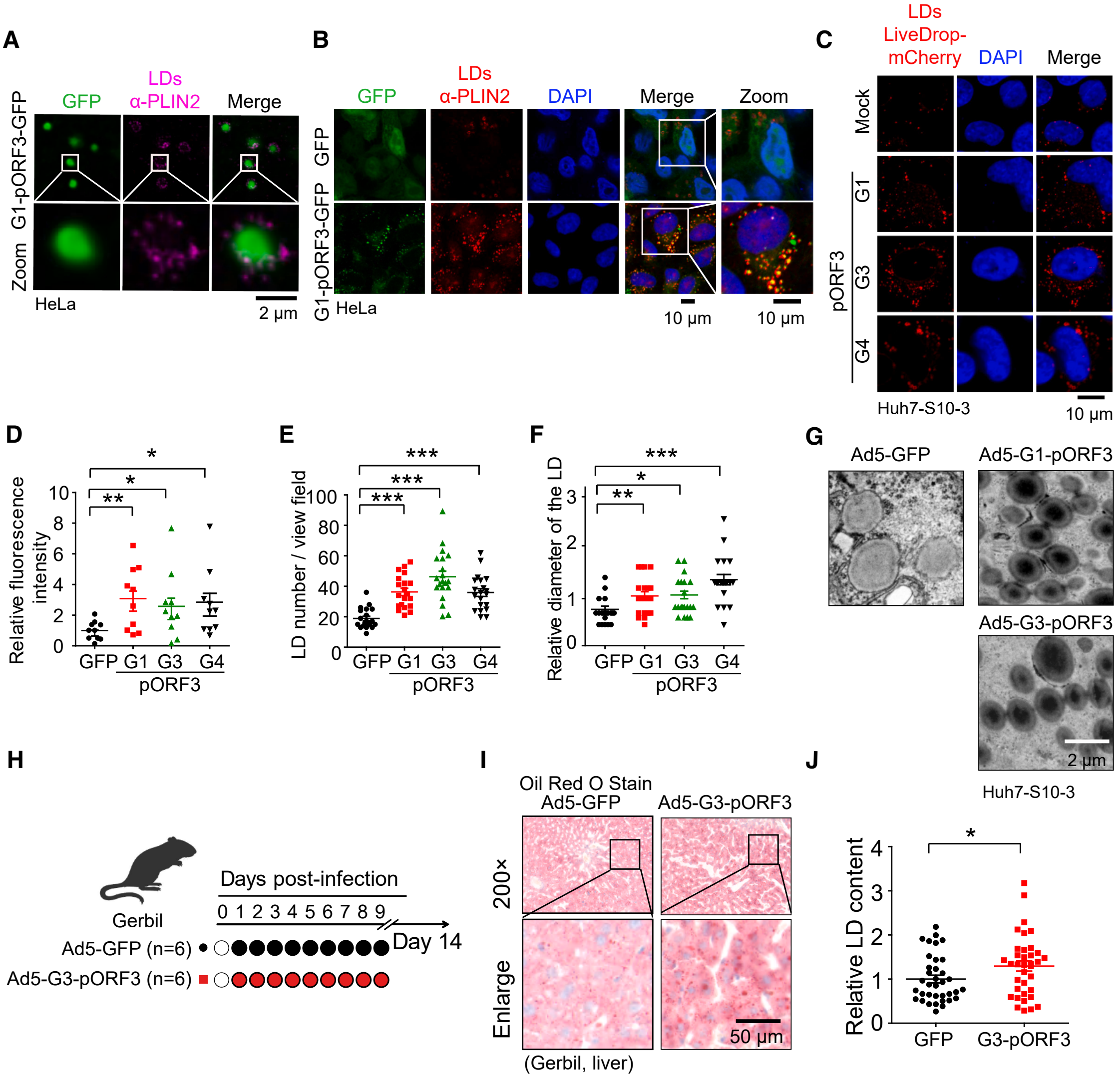

Figure 4. pORF3 associates with LDs and induces LD biogenesis *in vitro* and in gerbil livers

(A) Super-resolution stimulated emission depletion (STED) microscopy revealed the colocalization of G1-pORF3 with LDs marked by PLIN2. Scale bars, 2 μm.

(B) Immunofluorescence staining for PLIN2, a marker of LDs, confirmed that G1-pORF3 colocalizes with LDs. Scale bars, 10 μm.

(C–F) Confocal microscopy exhibited the increased LDs in Huh7-S10-3 cells infected with adenoviruses expressing G1-pORF3, G3-pORF3, and G4-pORF3 (Ad5-G1-pORF3, Ad5-G3-pORF3, and Ad5-G4-pORF3), compared to cells infected with an adenovirus expressing GFP (Ad5-GFP) (C) and confirmed by the statistical analyses of LD number, relative fluorescence intensity, and diameter (D–F). Data were analyzed using a one-way ANOVA test with Bonferroni correction. Scale bars, 10 μm. *$p < 0.05$, **$p < 0.01$, ***$p < 0.001$.

(G) Electron microscopy shows that Ad5-G1-pORF3 and Ad5-G3-pORF3 trigger increased Huh7-S10-3 LDs compared to Ad5-GFP. Scale bars, 2 μm.

(H) Schematic representation of recombinant adenoviruses harboring GFP (as a control) and pORF3 infecting gerbils.

(I and J) Oil red O staining of liver sections from gerbils infected with Ad5-GFP and Ad5-pORF3 (I) was analyzed using statistics (J) (six microscopic fields from each gerbil were randomly selected for statistical analysis). Data were analyzed using a one-way ANOVA test with Bonferroni correction. Scale bars, 50 μm. *$p < 0.05$.

immunoblotting (Figure 5A). Noticeably, live cell imaging recorded G1 and G3 pORF3 variants with the LLPS-like behavior, with clearly visible fusion of pORF3 puncta (Figure 5B). Live-cell imaging shows that G1-pORF3 condensates can fuse (Video S1), as time-stamped frames with tracks and line-scans capture droplet-droplet fusion rather than focus drift. Fluorescence recovery after photo bleaching (FRAP) assays found that laser-bleached pORF3 condensates gradually recovered their fluorescence intensity to pre-bleaching levels during complete or partial bleaching (Figures 5C and S4B). A slow pORF3 recovery is consistent with LD-surface constraints and indicates a fluid-like property of pORF3 puncta.

pORF3 is a compact viral protein with 113 or 114 amino acids, dividing into N-terminal hydrophobic domains (D1 and D2) for potential membrane and cytoskeleton interaction,[38] central proline-rich regions (P1 and P2) for protein interaction,[39] and C-terminal

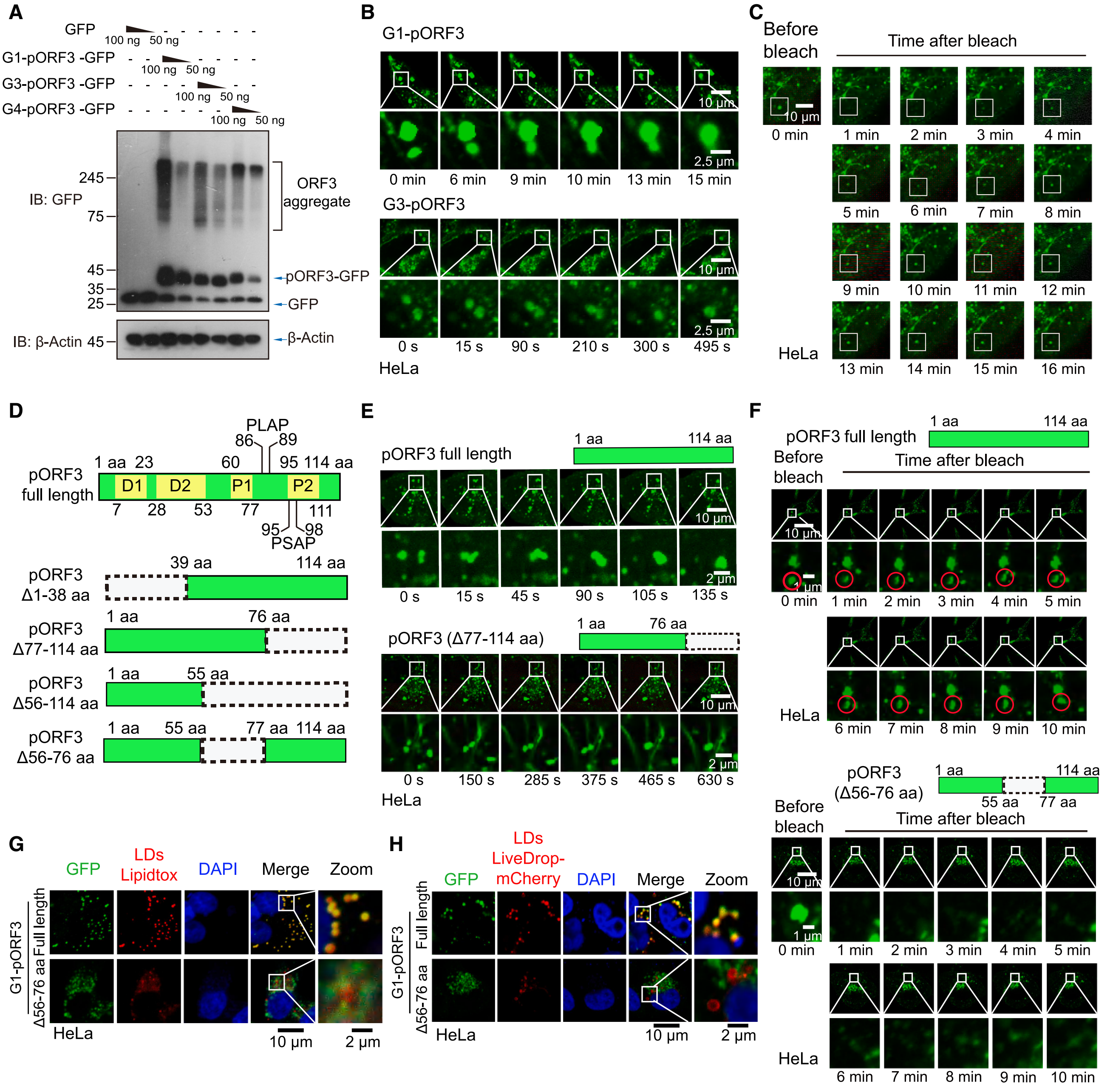

Figure 5. pORF3 forms phase separation to facilitate lipid anabolism

(A) pORF3 from all three HEV genotypes formed protein aggregates in a dose-dependent manner.

(B) Live-cell imaging with tracks and line scans recorded the fusion but not the z-drift of G1 and G3 pORF3 condensates, suggesting their fluid-like properties. Scale bars, 10 μm for original image; 2.5 μm for zoomed image.

(C) Time-lapse images of live-cell HEV-pORF3-GFP droplets captured immediately before and 16 min after complete photobleaching. Scale bars, 10 μm.

(D) Schematic representation of pORF3 truncations (Δ1–38, Δ77–114, Δ56–114, and Δ56–76); their subcellular localizations and aggregations were displayed in fluorescence microscopy.

(E) Live-cell confocal microscopy showed the fusion of pORF3 puncta, including those with full-length pORF3 and Δ77–114 truncation. Scale bars, 10 μm for original image; 2 μm for zoomed image.

(F) FRAP analyses revealed that pORF3 Δ56–76 truncation forfeited the fluorescence recovery capability after photobleaching. Scale bars, 10 μm for original image; 1 μm for zoomed image.

(G and H) Fluorescence microscopy analyses showed that the pORF3 Δ56–76 mutant lost the capacity to colocalize with LDs labeled by Lipidtox and LiveDrop-mCherry. Scale bars, 10 μm for original image; 2 μm for zoomed image.

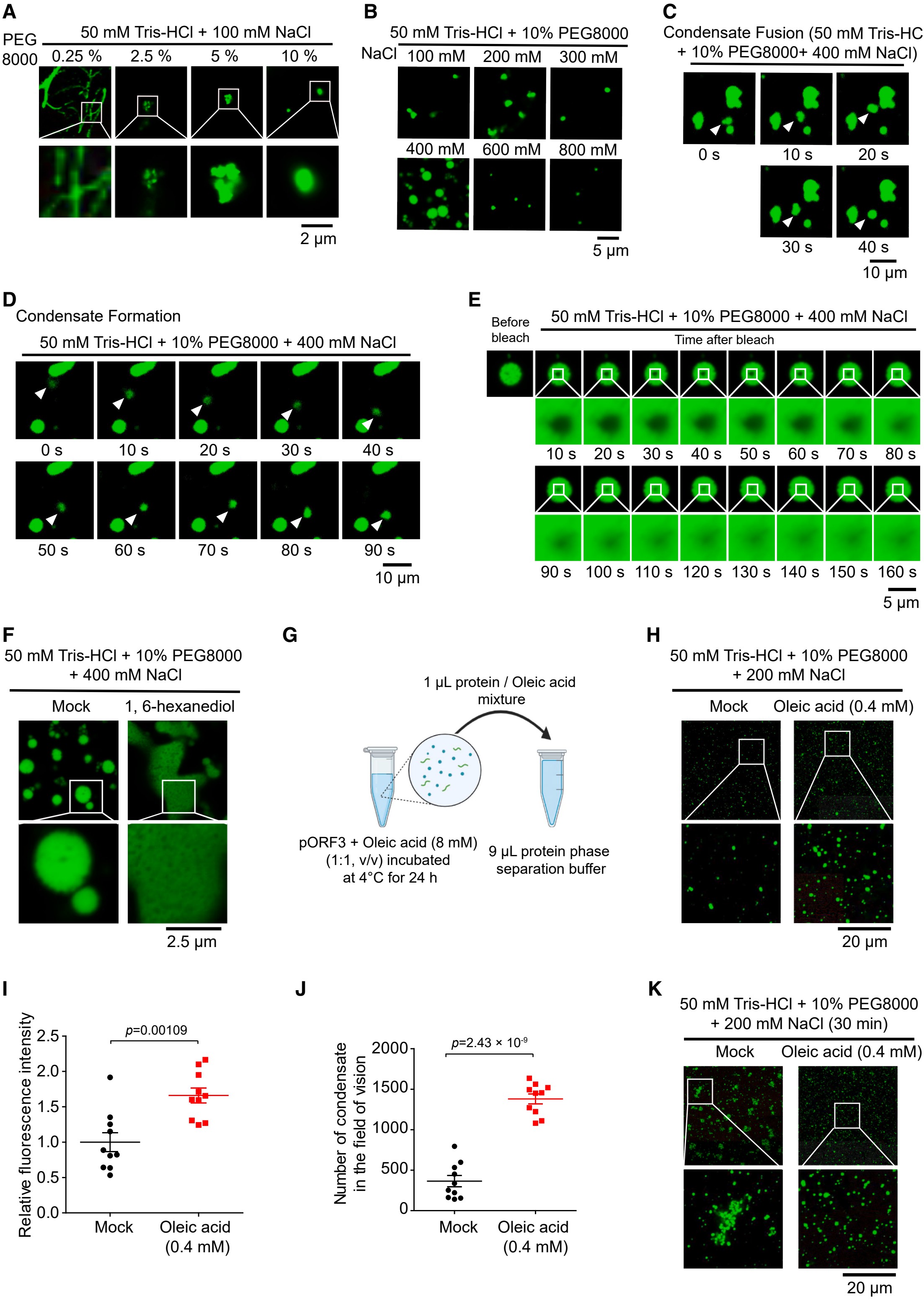

Figure 6. pORF3 exhibits LLPS-like properties *in vitro*

(A) Recombinant G1-pORF3-GFP was screened for droplet formation by titrating PEG-8000 (0.25%–10%) in 50 mM Tris-HCl, 400 mM NaCl. Scale bars, 2 μm.

(B) NaCl was varied at the optimal 10% PEG-8000 (100–800 mM) to refine the LLPS window. Scale bars, 5 μm.

(C and D) Confocal imaging under these conditions captured the dynamic fusion and maturation of pORF3 condensates. Scale bars, 10 μm.

(legend continued on next page)

PXXP motif and the viroporin region[10,40–42] (Figure 5D). Both PONDR and IUPred prediction suggest that pORF3 harbors intrinsically disordered regions (IDRs), mainly aa 38–76 and aa 88–114 (Figure S4C). To probe the structural determinants of pORF3 for LLPS, we generated stable cell lines expressing pORF3 WT and a series of pORF3 deletion mutants based on their IDR scores: Δ1–38, Δ77–114, Δ56–114, and Δ56–76 (Figure 5D). Both confocal and live-cell imaging suggest that condensates formed by the Δ77–114 truncation undergo fusion (Figure 5E; Video S2). By contrast, pORF3 Δ1–38 and Δ56–114 failed to form puncta, suggesting that aa 56–76 might be crucial for maintaining LLPS capability in pORF3 (Figures S4D and S4E). We then generated stable cells expressing pORF3 mutant (HeLa-pORF3-GFP Δ56–76). FRAP assays validated that this pORF3 deletion forfeited its fluid-like property (Figure 5F). Intriguingly, pORF3 Δ56–76 failed to colocalize with LDs labeling by LiveDrop-mCherry or Lipidtox (Figures 5G and 5H),and was excluded from LDs (Figure S4F), suggesting that the association of pORF3 with LDs might be attributed to its LLPS characteristics. We attempted to differentiate the LLPS property from the potential LD docking information in the pORF3 aa 56–76 region. However, pORF3-P3A, by which three prolines (P55, P59, and P64) were replaced with alanines, still had an intact LLPS ability (Figure S4G). Besides, we revealed that LLPS is a unique property of pORF3, but not a universal feature of lipid droplet-associated proteins (Figure S4H). These observations collectively suggest that the LLPS property of pORF3 is critical for its effective association with LDs and the formation of a unique virus-induced LD architecture.

pORF3 exhibits LLPS-like properties *in vitro*

We found that recombinant pORF3 forms phase-separated droplets under simple biochemical conditions. In 50 mM Tris-HCl, 400 mM NaCl, and 10% PEG-8000, confocal microscopy shows spherical condensates of pORF3 that fuse and relax into larger droplets, a hallmark of LLPS (Figures 6A–6D). FRAP assay reveals rapid signal return, and the droplets dissolve in 1,6-hexanediol (Figures 6E and 6F), indicating that weak, reversible interactions sustain them. Intriguingly, a lipid environment, which provides a hydrophobic interface, significantly facilitates LLPS of pORF3. Adding 0.4 mM oleic acid in a slightly lower-salt buffer (200 mM NaCl), which modestly lowers surface tension and tests the sensitivity of pORF3 condensation to hydrophobic cues, boosts fluorescence intensity and droplet number of pORF3 (Figures 6G–6J). After 30 min, the observation under current conditions showed that the oleic-acid droplets remain dynamic and show no irreversible aggregation, unlike untreated controls (Figure 6K). These preliminary assays suggest pORF3 as intrinsically capable of LLPS *in vitro* and identify that a lipid cue promotes its phase transition.

pORF3 promotes the expression of cholesterol synthesis genes

To investigate the role of pORF3 motifs in modulating lipid metabolism, we performed targeted lipid mass spectrometry analyses on cells stably expressing full-length and truncated versions of pORF3 with independent biological replicates. PCA revealed a substantial separation of lipid profiles among GFP, pORF3 WT, Δ77–114, Δ56–114, and Δ56–76 groups (Figures 7A and S5C). Specifically, the wild-type pORF3 group exhibited significantly higher TAG and CE levels compared to the Δ56–76, Δ77–114, and Δ56–114 mutant groups (Figures 7B, 7C, S5A, S5B, and S5D–S5G). The heatmap of these neutral lipid species also supported this observation, suggesting that the full-length pORF3, but not its Δ56–76, Δ77–114, or Δ56–114 deletions, induces a substantial accumulation in TAG or CE (Figures 7D and S5H).

Transcriptome analyses were followed to understand mechanisms through which pORF3 regulates lipid metabolism, which revealed that 324 genes were upregulated and 155 genes were downregulated in the pORF3 group (Figure 7E). Gene expression profiling between GFP and pORF3 groups and with three biological replicates per group confirmed its reliability and reproducibility (Figure 7F). Unbiased pathway enrichment analysis in the transcriptome data among 95 metabolic pathways identified cholesterol metabolism as the most significantly enriched pathway in pORF3-expressing cells (Figure S5I). Notably, transcriptome analyses identified significant alterations in the cholesterol metabolism pathways upon pORF3 expression in the Kandutsch-Russell pathway (Figures 7G and 7H). RT-qPCR validated the alterations of mRNA levels for some key cholesterol synthesis genes, such as MVD, ACSL1, HMGCS1, FADS1, and LSS, which were significantly upregulated by pORF3 (Figures 7I–7M). Expectedly, we found that authentic HEV infection similarly resulted in a significant increase in these key cholesterol genes in mRNA levels (Figures 7N–7R). These collective observations suggest that pORF3 induces an enhanced expression program of cholesterol synthesis genes, which likely contributes to LD biogenesis.

DISCUSSION

HEV is a zoonotic pathogen of significant concern and an ongoing public threat, particularly due to its high mortality rates in pregnant women[1] and a 10% rate of liver cirrhosis conversion within 2 years in chronic infection.[43] While typically associated with hepatitis, characterized by inflammation and liver damage within hepatocytes and bile duct cells,[44] HEV infection can also manifest in extrahepatic sites,[45] highlighting its potential for systemic impact. Given the significant public health threat

(E) FRAP shows rapid fluorescence recovery, confirming liquid behavior. Scale bars, 5 μm.

(F) Droplets dissolve in 5% 1,6-hexanediol, indicating reliance on weak hydrophobic interactions. Scale bars, 2.5 μm.

(G) Schematic of lipid modulation: pORF3 was pre-incubated with 8 mM oleic acid (1:1 v/v, 4°C, 24 h), and 1 μL of the mixture was added to the assay buffer.

(H and I) Fluorimetric and imaging analyses (50 mM Tris-HCl, 10% PEG-8000, 200 mM NaCl) reveal a marked increase in droplet intensity upon 0.4 mM oleate. Data were analyzed using a one-way ANOVA test with Bonferroni correction. Scale bars, 20 μm.

(J) ImageJ quantification confirms higher condensate counts in oleate-treated samples versus mock. Data were analyzed using a one-way ANOVA test with Bonferroni correction.

(K) After 30 min, oleate-induced droplets remain liquid, and no secondary aggregation is observed under these conditions. Scale bars, 20 μm.

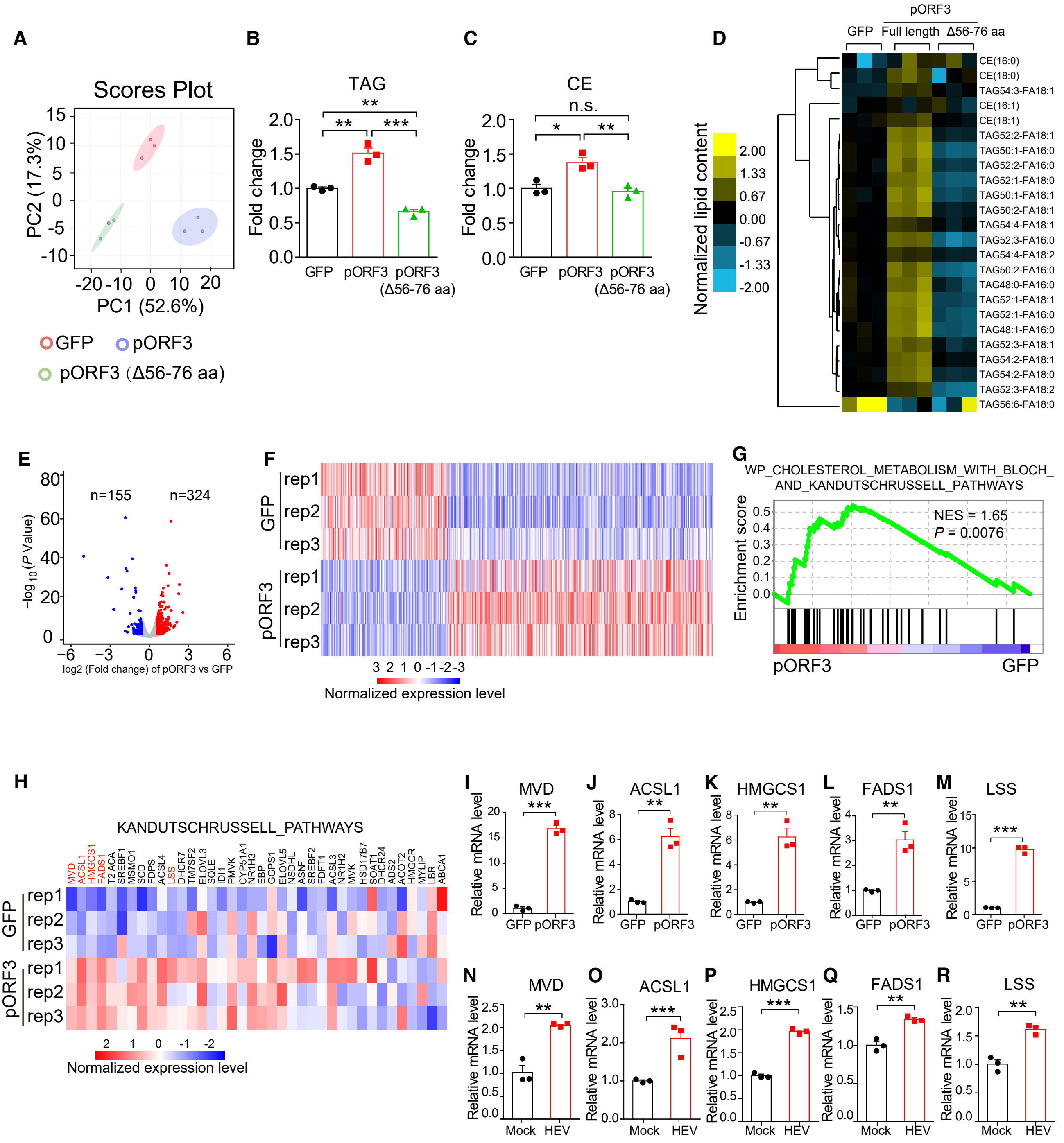

Figure 7. pORF3 promotes the expression of cholesterol synthesis genes

(A) Targeted lipidomics analyses separated GFP, full-length pORF3, and pORF3 Δ56–76 into distinct clusters in the score plot, indicating differential lipid profiles associated with pORF3 containing LLPS capability or not.

(B and C) Statistical analyses revealed a compromised increase in the relative abundance of TAG and CE in the pORF3 Δ56–76 mutant, compared with pORF3 full-length. Data were analyzed using a one-way ANOVA test with Bonferroni correction. $^*p < 0.05$, $^{**}p < 0.01$, $^{***}p < 0.001$; ns, not significant.

(D) Heatmaps of lipid metabolism visually highlighted the lipid anabolic differences among the various groups. The top 20 most abundant TAG species (ranked by lipidomic abundance) and all four detected CE species were selected for heatmap generation, $n = 3$.

(E) A scatterplot of transcriptome analysis compared the mRNAs between HeLa cells stably expressing pORF3 (HeLa-pORF3) and GFP, which were generated using a pBoBi-based strategy. mRNAs with greater than 2-fold changes in abundance in HeLa-pORF3 samples are highlighted in blue (decreased) and red (increased). The criterion for evaluating significance is a ≥1.5-fold change cutoff, p value < 0.05 threshold (unpaired two-tailed t test) to define significance.

(legend continued on next page)

posed by HEV, particularly its severe outcomes in vulnerable populations and systemic manifestations, many recent studies have focused on identifying a series of potential antiviral drugs to combat HEV infection.[46–51] The viral protein pORF3 has emerged as a critical virulence factor, playing a multifaceted role in modulating host immunity, facilitating viral release, and promoting the formation of eHEV.[10,11,52,53] Understanding the mechanisms by which pORF3 exerts these effects is crucial to understanding HEV pathogenicity and developing effective antiviral strategies.

LDs, dynamic organelles involved in lipid storage and metabolism, have been implicated in the life cycle of some viral pathogens, including HCV, DENV, and PV.[22–25] The diverse ways viruses exploit LDs have been reported for various stages of their replication cycle, including viral entry, replication, assembly, and egress.[54] Furthermore, recent research has positioned LDs as crucial regulators of the innate immune responses against pathogen invasion in mammals,[55] emphasizing the complex interplay between LDs, viral infection, and host immunity. Building on our observations of pORF3-driven LD biogenesis in HEV, we note that LDs serve as central hubs across diverse hepatitis viruses: HCV repurposes LD membranes via NS5A-core interactions to nucleate replication and assemble virions,[56] HBV perturbs cholesterol esterification and LD accumulation in both hepatocytes and CD8$^+$ T cells to facilitate egress and modulate immune responses,[57] and epidemiological data in HAV/HBV co-infection link fatty-liver disease to accelerated fibrosis.[58] Moreover, high-fat diets exacerbate steatosis and impair antiviral immunity, underlying how nutritional status and LD turnover intersect to influence infectious liver disease outcomes.

To investigate this intricate relationship between HEV and lipid metabolism, we utilized the Mongolian gerbil HEV model and the HEV RNA replicon cell line, both valuable tools in HEV research.[30,59–62] In the gerbil infection model, we observed a striking increase in viral titers in the livers and feces of animals fed a high-fat diet before HEV infection compared to those receiving a standard diet, suggesting that a high-fat diet creates a more favorable environment for HEV replication, potentially by altering lipid metabolism and immune responses. Despite the increased viral load, the high-fat diet group exhibited reduced liver damage compared to the standard diet group. This seemingly paradoxical observation led us to hypothesize that increased LDs in the high-fat diet group might sequester pORF3, mitigating its cytotoxic effects, which warrants further investigation. HEV infection mobilizes lipids into the bloodstream, decreasing hepatic LDs, indicating that the virus actively promotes LD biogenesis to replenish this crucial resource and sustain its infectivity. It is currently unclear whether phospholipids or sphingolipids produced in lipid metabolism are also impacted by HEV infection. Further investigation is also warranted to determine if these changes in lipid profiles at a systemic level could influence HEV pathogenesis. Notably, we found that pharmacological inhibition of LD biogenesis could be a viable therapeutic approach.

Using a multifaceted approach, including stable cell lines expressing pORF3, a pORF3 overexpression system, and genuine HEV infection, we confirmed that pORF3 increases LDs both *in vitro* and *in vivo*. In cultured hepatoma cells, virion release of HEV is inefficient, with less than 10% of total genome copies found in supernatant.[9] As such, intracellular lipids are not siphoned off for membrane envelopment, and consequently, the LD-building activity of pORF3 becomes dominant, yielding the robust LD expansion. We speculate that LDs supply the neutral-lipid pool required for eHEV assembly, provide energy substrates that sustain long-term replication, and may potentially maintain a replication niche in LD-consuming hepatocytes.

Mechanistically, pORF3 upregulates triacylglycerol and cholesterol ester levels, the main components of LDs, probably through promoting the expression of genes involved in cholesterol synthesis and via regulation of mitochondria-associated lipid metabolic pathways, such as SREBP and Peroxisome Proliferator-Activated Receptors (PPARs).[63,64] Studies have shown that viral proteins can upregulate the transcription of fat synthesis genes. For example, the X protein of HBV promotes hepatic steatosis by transcriptionally activating SREBP1 and PPARγ,[65] while the core protein of HCV genotype-3a upregulates the fatty acid synthase promoter.[66] It is currently unknown whether pORF3 interacts directly with host factors to mediate LD biogenesis function. LDs bud from the ER as nascent neutral-lipid lenses surrounded by a phospholipid monolayer. pORF3 is co-translationally palmitoylated by endoplasmic reticulum (ER)/Golgi-resident Zinc finger DHHC domain-containing protein (ZDHHC) enzymes,[67] recruiting it to the ER membrane. We speculate that pORF3 likely associates transiently with ER membranes during palmitoylation before relocating to LDs.

Intriguingly, we uncovered a novel aspect of pORF3, i.e., its capacity to undergo LLPS. Fluorescence microscopy imaging revealed that pORF3 forms puncta, and live-cell imaging and photobleaching experiments confirmed the dynamic properties of these condensates. LLPS is a phenomenon by which proteins condense into distinct membrane-less compartments within the cell, and it has been increasingly recognized as a crucial mechanism for regulating various cellular processes.[68] The capacity of pORF3 undergoing LLPS plays a key role in its interaction with and modulation of LDs. Specifically, we identified the 56–76 amino acid region as an essential motif for pORF3 LLPS. Targeted lipid mass spectrometry showed that compared with the WT-pORF3, pORF3 (Δ56–76 aa) could not upregulate TAG and CE. Oleic acid, which produces a lipid cue *in vitro*, promoted

---

(F) The transcriptome assay was performed in HeLa cells with stable expression of G1-pORF3 and GFP and depicted by the heatmap for the patterns of mRNA expression.

(G) Gene set enrichment analysis (GSEA) plots showed that mRNAs associated with pORF3 are enriched in the cholesterol metabolism pathway, suggesting that pORF3 promotes the transcription or translation of genes involved in cholesterol synthesis.

(H–M) The heatmap of cholesterol-metabolism genes shows five significantly upregulated targets (in red), including MVD, ACSL1, HMGCS1, FADS1, and LSS, which were selected for validation by RT-qPCR.

(N–R) RT-qPCR analyses validated the increased mRNA levels of MVD, ACSL1, HMGCS1, FADS1, and LSS in genuine HEV-infected Huh7-S10-3 compared to the controls. Data were analyzed using a one-way ANOVA test with Bonferroni correction. $^{**}p < 0.01$, $^{***}p < 0.001$.

the formation of pORF3 condensates and modulated their dynamic aggregation states. The colocalization of pORF3 with LD-surface markers (PLIN2) confirms its structural integration. BODIPY staining reveals that pORF3 condensates contain neutral lipids. Oleic acid modulates pORF3 condensate formation, suggesting pORF3 may bridge LD biology and condensate dynamics. These data are consistent with a model in which pORF3 undergoes LLPS to generate condensates that partially associate with the LD phospholipid monolayer. This surface-bound condensate explains why the assemblies exhibit properties of both membrane-less condensates and LD-proximal structures. This lipid-dependent behavior might distinguish pORF3 assembly from canonical protein-nucleic acid condensates, revealing an intriguing mechanism by which HEV co-opts host lipids.

In conclusion, this study reveals the nature of phase separation and a novel function of pORF3 in regulating LD biogenesis and highlights its multifaceted role in HEV infection. Our findings propose a complex interplay between HEV and lipid metabolism, offering potential therapeutic targets for combating this significant human pathogen.

Limitations of the study

Although our data implicate LDs in the HEV life cycle, the precise step(s) they support, such as viral genome replication, particle assembly, or egress, remain unresolved, and real-time mechanistic studies will be needed to clarify their contribution. Our localization model favors LD-surface (interfacial) condensates formed by pORF3, and the Δ56–76 mutant deletes a segment that probably harbors LD-targeting signals, LD docking, and phase-separation determinants. Diffraction-limited imaging cannot exclude shallow penetration into interfacial defects. Therefore, super-resolution/electron microscopy (EM) and structure-guided mutagenesis will be needed to refine these points. Some experiments used non-hepatic cell lines, an adenoviral expression system, and epitope tags (GFP/FLAG), which did not reconstitute the infectious HEV cycle. Investigation *in vivo* and with untagged/minimally tagged pORF3 is needed. Specific controls could refine *in vitro* LLPS data and oleic acid assay screens for hydrophobic cues. Finally, our lipid-metabolic profiling was confined to a single acute time point (day 14 post-infection). Long-term effects of chronic HEV infection and potential drug pleiotropy remain to be defined.

RESOURCE AVAILABILITY

Lead contact

Further information and requests for reagents may be directed to and will be fulfilled by the lead contact, Pinglong Xu (xupl@zju.edu.cn).

Materials availability

This study did not generate new or unique reagents.

Data and code availability

All data supporting the findings of this study are available in this manuscript and from the corresponding authors upon reasonable request. Statistical source data for Figures 1, 2, 3, 4, 5, 6, 7, S1, S2, S3, S4, and S5 are provided in Table S1, and unprocessed images of the blots are shown in Figure S6. The targeted lipid mass spectrometry data are shown in Table S2. Detailed information about primers can be found in Table S3. A list of plasmids is provided in the accompanying Table S4. Live-cell imaging of G1-pORF3 WT and Δ77–114 condensates is shown in Videos S1 and S2. The lead contact will share all data reported in this paper upon reasonable request. RNA-seq data (GEO: GSE299317) are available in NCBI (https://www.ncbi.nlm.nih.gov/). This paper does not report original code. Any additional information required to reanalyze the data reported in this paper is available from the lead contact upon request.

ACKNOWLEDGMENTS

This research was sponsored by the National Natural Science Foundation of China (NSFC) Project (32321002, 32430028, and 31830052 to P.X., and 92269105 and U22A20521 to Y.-W.H.), the State Key Laboratory for Diagnosis and Treatment of Infectious Diseases (zz202403), the Laboratory of Lingnan Modern Agriculture Project (NG2022001 to Y.-W.H.), and the Zhejiang University Experimental Technology Research Project (General Project) (SYBJS202532 to L.-D.X.).

AUTHOR CONTRIBUTIONS

L.-D.X. and F.Z. carried out most of the experiments; C.M., X.Y., Y.Z., M.-D.Z., and S.L. performed some experiments; S.S., Q.S., D.N., Q.Z., L.S., T.L., and C. Y. helped with experimental resources, data analyses, and discussions; P.X., Y.-W.H., and L.-D.X. conceived the study and experimental design; P.X., L.-D. X., and Y.-W.H. wrote the manuscript.

DECLARATION OF INTERESTS

The authors declare no competing interests.

STAR★METHODS

Detailed methods are provided in the online version of this paper and include the following:

- KEY RESOURCES TABLE
- METHOD DETAILS
  - ○ Mammalian cell lines and transfections
  - ○ Expression plasmids, reagents, and antibodies
  - ○ Viruses
  - ○ Quantitative RT-PCR assay
  - ○ Immunofluorescence and microscopy
  - ○ Electron microscopy analysis
  - ○ STED super-resolution microscopy
  - ○ HE and Oil Red O staining
  - ○ RNA-seq data analysis
  - ○ Lipid extraction from tissue
  - ○ Lipid extraction for cell and quantification by mass spectrometry
  - ○ Recombinant protein expression and purification
  - ○ High-fat diet and cholesterol regulation
  - ○ Gerbil infection of HEV WT and HEV-null-ORF3
  - ○ Adenovirus infection in gerbils
- QUANTIFICATION AND STATISTICAL ANALYSIS
  - ○ Statistics and reproducibility
  - ○ LD quantification
- ADDITIONAL RESOURCES

SUPPLEMENTAL INFORMATION

Supplemental information can be found online at https://doi.org/10.1016/j.celrep.2025.116406.

Received: February 10, 2025
Revised: June 30, 2025
Accepted: September 18, 2025

REFERENCES

1. Sooryanarain, H., and Meng, X.J. (2019). Hepatitis E virus: reasons for emergence in humans. Curr. Opin. Virol. *34*, 10–17. https://doi.org/10.1016/j.coviro.2018.11.006.
2. Meng, X.J. (2016). Expanding Host Range and Cross-Species Infection of Hepatitis E Virus. PLoS Pathog. *12*, e1005695. https://doi.org/10.1371/journal.ppat.1005695.
3. Nimgaonkar, I., Ding, Q., Schwartz, R.E., and Ploss, A. (2018). Hepatitis e virus: Advances and challenges. Nat. Rev. Gastroenterol. Hepatol. *15*, 96–110. https://doi.org/10.1038/nrgastro.2017.150.
4. Kenney, S.P., and Meng, X.J. (2019). Hepatitis E Virus Genome Structure and Replication Strategy. Cold Spring Harb. Perspect. Med. *9*, a031724. https://doi.org/10.1101/cshperspect.a031724.
5. Mahilkar, S., Paingankar, M.S., and Lole, K.S. (2016). Hepatitis E virus RNA-dependent RNA polymerase: RNA template specificities, recruitment and synthesis. J. Gen. Virol. *97*, 2231–2242. https://doi.org/10.1099/jgv.0.000528.
6. Yin, X., Ying, D., Lhomme, S., Tang, Z., Walker, C.M., Xia, N., Zheng, Z., and Feng, Z. (2018). Origin, antigenicity, and function of a secreted form of ORF2 in hepatitis E virus infection. Proc. Natl. Acad. Sci. USA *115*, 4773–4778. https://doi.org/10.1073/pnas.1721345115.
7. LeDesma, R., Heller, B., Biswas, A., Maya, S., Gili, S., Higgins, J., and Ploss, A. (2023). Structural features stabilized by divalent cation coordination within hepatitis E virus ORF1 are critical for viral replication. eLife *12*, e80529. https://doi.org/10.7554/eLife.80529.
8. Zhang, F., Xu, L.-D., Wu, S., Wu, Q., Wang, A., Liu, S., Zhang, Q., Yu, X., Wang, B., Pan, Y., et al. (2025). Proteasomal processing of the viral replicase ORF1 facilitates HEV-induced liver fibrosis. Proc. Natl. Acad. Sci. USA *122*, e2419946122. https://doi.org/10.1073/pnas.2419946122.
9. Yin, X., Ambardekar, C., Lu, Y., and Feng, Z. (2016). Distinct entry mechanisms for nonenveloped and quasi-enveloped hepatitis E viruses. J. Virol. *90*, 4232–4242. https://doi.org/10.1128/JVI.02804-15.
10. Ding, Q., Heller, B., Capuccino, J.M.V., Song, B., Nimgaonkar, I., Hrebikova, G., Contreras, J.E., and Ploss, A. (2017). Hepatitis e virus ORF3 is a functional ion channel required for release of infectious particles. Proc. Natl. Acad. Sci. USA *114*, 1147–1152. https://doi.org/10.1073/pnas.1614955114.
11. Sari, G., Zhu, J., Ambardekar, C., Yin, X., Boonstra, A., Feng, Z., and Vanwolleghem, T. (2021). The viral orf3 protein is required for hepatitis e virus apical release and efficient growth in polarized hepatocytes and humanized mice. J. Virol. *95*, e0058521. https://doi.org/10.1128/JVI.00585-21.
12. Surjit, M., Oberoi, R., Kumar, R., and Lal, S.K. (2006). Enhanced alpha1 microglobulin secretion from Hepatitis E virus ORF3-expressing human hepatoma cells is mediated by the tumor susceptibility gene 101. J. Biol. Chem. *281*, 8135–8142. https://doi.org/10.1074/jbc.M509568200.
13. Liu, X., Liu, T., Shao, Z., Xiong, X., Qi, S., Guan, J., Wang, M., Tang, Y.D., Feng, Z., Wang, L., and Yin, X. (2025). Palmitoylation-dependent association with Annexin II directs hepatitis E virus ORF3 sorting into vesicles and quasi-enveloped virions. Proc. Natl. Acad. Sci. USA *122*, e2418751122. https://doi.org/10.1073/pnas.2418751122.
14. Okamoto, H. (2013). Culture systems for hepatitis E virus. J. Gastroenterol. *48*, 147–158. https://doi.org/10.1007/s00535-012-0682-0.
15. Olzmann, J.A., and Carvalho, P. (2019). Dynamics and functions of lipid droplets. Nat. Rev. Mol. Cell Biol. *20*, 137–155. https://doi.org/10.1038/s41580-018-0085-z.
16. Thiam, A.R., Farese, R.V., Jr., and Walther, T.C. (2013). The biophysics and cell biology of lipid droplets. Nat. Rev. Mol. Cell Biol. *14*, 775–786. https://doi.org/10.1038/nrm3699.
17. Mathiowetz, A.J., and Olzmann, J.A. (2024). Lipid droplets and cellular lipid flux. Nat. Cell Biol. *26*, 331–345. https://doi.org/10.1038/s41556-024-01364-4.
18. Martin, S., and Parton, R.G. (2006). Lipid droplets: A unified view of a dynamic organelle. Nat. Rev. Mol. Cell Biol. *7*, 373–378. https://doi.org/10.1038/nrm1912.
19. Fei, W., and Yang, H. (2012). Genome-Wide Screens for Gene Products Regulating Lipid Droplet Dynamics. In Methods in Cell Biology (Academic Press Inc.), pp. 303–316. https://doi.org/10.1016/B978-0-12-386487-1.00014-6.
20. Gluchowski, N.L., Becuwe, M., Walther, T.C., and Farese, R.V. (2017). Lipid droplets and liver disease: From basic biology to clinical implications. Nat. Rev. Gastroenterol. Hepatol. *14*, 343–355. https://doi.org/10.1038/nrgastro.2017.32.
21. Hattori, N., Arano, T., Hatano, T., Mori, A., and Imai, Y. (2017). Mitochondrial-Associated Membranes in Parkinson's Disease. In Organelle Contact Sites: From Molecular Mechanism to Disease, M. Tagaya and T. Simmen, eds. (Springer Singapore), pp. 157–169. https://doi.org/10.1007/978-981-10-4567-7_12.
22. Shimotohno, K. (2021). HCV assembly and egress via modifications in host lipid metabolic systems. Cold Spring Harb. Perspect. Med. *11*, a036814. https://doi.org/10.1101/cshperspect.a036814.
23. Miyanari, Y., Atsuzawa, K., Usuda, N., Watashi, K., Hishiki, T., Zayas, M., Bartenschlager, R., Wakita, T., Hijikata, M., and Shimotohno, K. (2007). The lipid droplet is an important organelle for hepatitis C virus production. Nat. Cell Biol. *9*, 1089–1097. https://doi.org/10.1038/ncb1631.
24. Samsa, M.M., Mondotte, J.A., Iglesias, N.G., Assunção-Miranda, I., Barbosa-Lima, G., Da Poian, A.T., Bozza, P.T., and Gamarnik, A.V. (2009). Dengue virus capsid protein usurps lipid droplets for viral particle formation. PLoS Pathog. *5*, e1000632. https://doi.org/10.1371/journal.ppat.1000632.
25. Laufman, O., Perrino, J., and Andino, R. (2019). Viral Generated Inter-Organelle Contacts Redirect Lipid Flux for Genome Replication. Cell *178*, 275–289.e16. https://doi.org/10.1016/j.cell.2019.05.030.
26. Yamada, K., Takahashi, M., Hoshino, Y., Takahashi, H., Ichiyama, K., Nagashima, S., Tanaka, T., and Okamoto, H. (2009). ORF3 protein of hepatitis E virus is essential for virion release from infected cells. J. Gen. Virol. *90*, 1880–1891. https://doi.org/10.1099/vir.0.010561-0.
27. Liao, J.K., and Laufs, U. (2005). Pleiotropic effects of statins. Annu. Rev. Pharmacol. Toxicol. *45*, 89–118. https://doi.org/10.1146/annurev.pharmtox.45.120403.095748.
28. Horton, J.D., Goldstein, J.L., and Brown, M.S. (2002). SREBPs: activators of the complete program of cholesterol and fatty acid synthesis in the liver. J. Clin. Investig. *109*, 1125–1131. https://doi.org/10.1172/jci200215593.
29. Sheng, Y., Deng, Y., Li, X., Ji, P., Sun, X., Liu, B., Zhu, J., Zhao, J., Nan, Y., Zhou, E.M., et al. (2024). Hepatitis E virus ORF3 protein hijacking thioredoxin domain-containing protein 5 (TXNDC5) for its stability to promote viral particle release. J. Virol. *98*, e0164923. https://doi.org/10.1128/jvi.01649-23.
30. Xu, L.D., Zhang, F., Peng, L., Luo, W.T., Chen, C., Xu, P., and Huang, Y.W. (2020). Stable Expression of a Hepatitis E Virus (HEV) RNA Replicon in Two Mammalian Cell Lines to Assess Mechanism of Innate Immunity and Antiviral Response. Front. Microbiol. *11*, 603699. https://doi.org/10.3389/fmicb.2020.603699.
31. Zhang, F., Xu, L.D., Zhang, Q., Wang, A., Yu, X., Liu, S., Chen, C., Wu, S., Jin, J., Lin, A., et al. (2023). Targeting proteostasis of the HEV replicase to combat infection in preclinical models. J. Hepatol. *78*, 704–716. https://doi.org/10.1016/j.jhep.2022.12.010.
32. Huang, Y.W., Opriessnig, T., Halbur, P.G., and Meng, X.J. (2007). Initiation at the third in-frame AUG codon of open reading frame 3 of the hepatitis E virus is essential for viral infectivity in vivo. J. Virol. *81*, 3018–3026. https://doi.org/10.1128/jvi.02259-06.
33. Yin, X., Li, X., Ambardekar, C., Hu, Z., Lhomme, S., and Feng, Z. (2017). Hepatitis E virus persists in the presence of a type III interferon response. PLoS Pathog. *13*, e1006417. https://doi.org/10.1371/journal.ppat.1006417.

34. Emerson, S.U., Nguyen, H., Torian, U., and Purcell, R.H. (2006). ORF3 protein of hepatitis E virus is not required for replication, virion assembly, or infection of hepatoma cells in vitro. J. Virol. *80*, 10457–10464. https://doi.org/10.1128/JVI.00892-06.

35. Wang, H., Becuwe, M., Housden, B.E., Chitraju, C., Porras, A.J., Graham, M.M., Liu, X.N., Thiam, A.R., Savage, D.B., Agarwal, A.K., et al. (2016). Seipin is required for converting nascent to mature lipid droplets. eLife *5*, e16582. https://doi.org/10.7554/eLife.16582.

36. Graff, J., Nguyen, H., Yu, C., Elkins, W.R., St Claire, M., Purcell, R.H., and Emerson, S.U. (2005). The open reading frame 3 gene of hepatitis E virus contains a cis-reactive element and encodes a protein required for infection of macaques. J. Virol. *79*, 6680–6689. https://doi.org/10.1128/jvi.79.11.6680-6689.2005.

37. Shin, Y., and Brangwynne, C.P. (2017). Liquid phase condensation in cell physiology and disease. Science *357*, eaaf4382. https://doi.org/10.1126/science.aaf4382.

38. Kannan, H., Fan, S., Patel, D., Bossis, I., and Zhang, Y.J. (2009). The hepatitis E virus open reading frame 3 product interacts with microtubules and interferes with their dynamics. J. Virol. *83*, 6375–6382. https://doi.org/10.1128/JVI.02571-08.

39. Tyagi, S., Jameel, S., and Lal, S.K. (2001). Self-association and mapping of the interaction domain of hepatitis E virus ORF3 protein. J. Virol. *75*, 2493–2498. https://doi.org/10.1128/jvi.75.5.2493-2498.2001.

40. Nagashima, S., Takahashi, M., Jirintai, Tanaka, T., Yamada, K., Nishizawa, T., and Okamoto, H. (2011). A PSAP motif in the ORF3 protein of hepatitis E virus is necessary for virion release from infected cells. J. Gen. Virol. *92*, 269–278. https://doi.org/10.1099/vir.0.025791-0.

41. Kenney, S.P., Wentworth, J.L., Heffron, C.L., and Meng, X.J. (2015). Replacement of the hepatitis E virus ORF3 protein PxxP motif with heterologous late domain motifs affects virus release via interaction with TSG101. Virology *486*, 198–208. https://doi.org/10.1016/j.virol.2015.09.012.

42. Emerson, S.U., Nguyen, H.T., Torian, U., Burke, D., Engle, R., and Purcell, R.H. (2010). Release of genotype 1 hepatitis E virus from cultured hepatoma and polarized intestinal cells depends on open reading frame 3 protein and requires an intact PXXP motif. J. Virol. *84*, 9059–9069. https://doi.org/10.1128/JVI.00593-10.

43. Thakur, V., Ratho, R.K., Kumar, S., Saxena, S.K., Bora, I., and Thakur, P. (2020). Viral Hepatitis E and Chronicity: A Growing Public Health Concern. Front. Microbiol. *11*, 577339. https://doi.org/10.3389/fmicb.2020.577339.

44. Mushahwar, I.K. (2008). Hepatitis E virus: Molecular virology, clinical features, diagnosis, transmission, epidemiology, and prevention. J. Med. Virol. *80*, 646–658. https://doi.org/10.1002/jmv.21116.

45. Kamar, N., Izopet, J., Pavio, N., Aggarwal, R., Labrique, A., Wedemeyer, H., and Dalton, H.R. (2017). Hepatitis E virus infection. Nat. Rev. Dis. Primers *3*, 17086. https://doi.org/10.1038/nrdp.2017.86.

46. Kamar, N., Garrouste, C., Haagsma, E.B., Garrigue, V., Pischke, S., Chauvet, C., Dumortier, J., Cannesson, A., Cassutoviguier, E., Thervet, E., et al. (2011). Factors associated with chronic hepatitis in patients with hepatitis e virus infection who have received solid organ transplants. Gastroenterology *140*, 1481–1489. https://doi.org/10.1053/j.gastro.2011.02.050.

47. Klöhn, M., Burkard, T., Janzen, J., Haase, J.A., Gömer, A., Fu, R., Ssebyatika, G., Nocke, M.K., Brown, R.J.P., Krey, T., et al. (2024). Targeting cellular cathepsins inhibits hepatitis E virus entry. Hepatology *80*, 1239–1251. https://doi.org/10.1097/HEP.0000000000000912.

48. Gömer, A., Klöhn, M., Jagst, M., Nocke, M.K., Pischke, S., Horvatits, T., Schulze Zur Wiesch, J., Müller, T., Hardtke, S., Cornberg, M., et al. (2023). Emergence of resistance-Associated variants during sofosbuvir treatment in chronically infected hepatitis e patients. Hepatology *78*, 1882–1895. https://doi.org/10.1097/HEP.0000000000000514.

49. Primadharsini, P.P., Nagashima, S., Nishiyama, T., and Okamoto, H. (2023). Three Distinct Reporter Systems of Hepatitis E Virus and Their Utility as Drug Screening Platforms. Viruses *15*, 1989. https://doi.org/10.3390/v15101989.

50. Qu, C., Li, Y., Li, Y., Yu, P., Li, P., Donkers, J.M., van de Graaf, S.F.J., de Man, R.A., Peppelenbosch, M.P., and Pan, Q. (2019). FDA-drug screening identifies deptropine inhibiting hepatitis E virus involving the NF-κB-RIPK1-caspase axis. Antiviral Res. *170*, 104588. https://doi.org/10.1016/j.antiviral.2019.104588.

51. Li, Y., Yu, P., Kessler, A.L., Shu, J., Liu, X., Liang, Z., Liu, J., Li, Y., Li, P., Wang, L., et al. (2022). Hepatitis E virus infection activates NOD-like receptor family pyrin domain-containing 3 inflammasome antagonizing interferon response but therapeutically targetable. Hepatology *75*, 196–212. https://doi.org/10.1002/hep.32114.

52. Nan, Y., Ma, Z., Wang, R., Yu, Y., Kannan, H., Fredericksen, B., and Zhang, Y.J. (2014). Enhancement of interferon induction by ORF3 product of Hepatitis E virus. J. Virol. *88*, 8696–8705. https://doi.org/10.1128/JVI.01228-14.

53. Nagashima, S., Jirintai, S., Takahashi, M., Kobayashi, T., Nishizawa, T., Nishizawa, T., Kouki, T., Yashiro, T., and Okamoto, H. (2014). Hepatitis E virus egress depends on the exosomal pathway, with secretory exosomes derived from multivesicular bodies. J. Gen. Virol. *95*, 2166–2175. https://doi.org/10.1099/vir.0.066910-0.

54. Jones, J.E., Le Sage, V., and Lakdawala, S.S. (2021). Viral and host heterogeneity and their effects on the viral life cycle. Nat. Rev. Microbiol. *19*, 272–282. https://doi.org/10.1038/s41579-020-00449-9.

55. Bosch, M., Sánchez-Álvarez, M., Fajardo, A., Kapetanovic, R., Steiner, B., Dutra, F., Moreira, L., López, J.A., Campo, R., Marí, M., et al. (2020). Mammalian lipid droplets are innate immune hubs integrating cell metabolism and host defense. Science *370*, 8085. https://doi.org/10.1126/science.aay8085.

56. Chatel-Chaix, L., and Bartenschlager, R. (2014). Dengue virus- and hepatitis C virus-induced replication and assembly compartments: the enemy inside–caught in the web. J. Virol. *88*, 5907–5911. https://doi.org/10.1128/jvi.03404-13.

57. Schmidt, N.M., Wing, P.A.C., Diniz, M.O., Pallett, L.J., Swadling, L., Harris, J.M., Burton, A.R., Jeffery-Smith, A., Zakeri, N., Amin, O.E., et al. (2021). Targeting human Acyl-CoA:cholesterol acyltransferase as a dual viral and T cell metabolic checkpoint. Nat. Commun. *12*, 2814. https://doi.org/10.1038/s41467-021-22967-7.

58. Vassilopoulos, S., Kalligeros, M., Vassilopoulos, A., Shehadeh, F., Benitez, G., Kaczynski, M., Lazaridou, I., Promrat, K., Wands, J.R., and Mylonakis, E. (2023). Impact of prior HBV, HAV, and HEV infection on non-alcoholic fatty liver disease. J. Viral Hepat. *30*, 685–693. https://doi.org/10.1111/jvh.13862.

59. Xu, L.D., Zhang, F., Chen, C., Peng, L., Luo, W.T., Chen, R., Xu, P., and Huang, Y.W. (2022). Revisiting the Mongolian Gerbil Model for Hepatitis E Virus by Reverse Genetics. Microbiol. Spectr. *10*, e0219321. https://doi.org/10.1128/spectrum.02193-21.

60. Liu, T., He, Q., Yang, X., Li, Y., Yuan, D., Lu, Q., Tang, T., Guan, G., Zheng, L., Zhang, H., et al. (2024). An Immunocompetent Mongolian Gerbil Model for Hepatitis E Virus Genotype 1 Infection. Gastroenterology *167*, 750–763.e10. https://doi.org/10.1053/j.gastro.2024.03.038.

61. Nimgaonkar, I., Archer, N.F., Becher, I., Shahrad, M., LeDesma, R.A., Mateus, A., Caballero-Gómez, J., Berneshawi, A.R., Ding, Q., Douam, F., et al. (2021). Isocotoin suppresses hepatitis E virus replication through inhibition of heat shock protein 90. Antiviral Res. *185*, 104997. https://doi.org/10.1016/j.antiviral.2020.104997.

62. Subramaniam, S., Fares-Gusmao, R., Sato, S., Cullen, J.M., Takeda, K., Farci, P., and McGivern, D.R. (2023). Distinct disease features of acute and persistent genotype 3 hepatitis E virus infection in immunocompetent and immunosuppressed Mongolian gerbils. PLoS Pathog. *19*, e1011664. https://doi.org/10.1371/journal.ppat.1011664.

63. Bertolio, R., Napoletano, F., Mano, M., Maurer-Stroh, S., Fantuz, M., Zannini, A., Bicciato, S., Sorrentino, G., and Del Sal, G. (2019). Sterol regulatory element binding protein 1 couples mechanical cues and lipid

metabolism. Nat. Commun. *10*, 1326. https://doi.org/10.1038/s41467-019-09152-7.

64. Soares, V.C., Dias, S.S.G., Santos, J.C., Azevedo-Quintanilha, I.G., Moreira, I.B.G., Sacramento, C.Q., Fintelman-Rodrigues, N., Temerozo, J. R., da Silva, M.A.N., Barreto-Vieira, D.F., et al. (2023). Inhibition of the SREBP pathway prevents SARS-CoV-2 replication and inflammasome activation. Life Sci. Alliance *6*, e202302049. https://doi.org/10.26508/lsa.202302049.
65. Kim, K.H., Shin, H.-J., Kim, K., Choi, H.M., Rhee, S.H., Moon, H.B., Kim, H. H., Yang, U.S., Yu, D.-Y., and Cheong, J. (2007). Hepatitis B virus X protein induces hepatic steatosis via transcriptional activation of SREBP1 and PPARγ. Gastroenterology *132*, 1955–1967. https://doi.org/10.1053/j.gastro.2007.03.039.
66. Jackel-Cram, C., Babiuk, L.A., and Liu, Q. (2007). Up-regulation of fatty acid synthase promoter by hepatitis C virus core protein: Genotype-3a core has a stronger effect than genotype-1b core. J. Hepatol. *46*, 999–1008. https://doi.org/10.1016/j.jhep.2006.10.019.
67. Lowther, J., Naismith, J.H., Dunn, T.M., and Campopiano, D.J. (2012). Structural, mechanistic and regulatory studies of serine palmitoyltransferase. Biochem. Soc. Trans. *40*, 547–554. https://doi.org/10.1042/bst20110769.
68. Spruijt, E. (2023). Open questions on liquid-liquid phase separation. Commun. Chem. *6*, 23. https://doi.org/10.1038/s42004-023-00823-7.
69. Shukla, P., Nguyen, H.T., Faulk, K., Mather, K., Torian, U., Engle, R.E., and Emerson, S.U. (2012). Adaptation of a genotype 3 hepatitis E virus to efficient growth in cell culture depends on an inserted human gene segment acquired by recombination. J. Virol. *86*, 5697–5707. https://doi.org/10.1128/JVI.00146-12.
70. Cordoba, L., Feagins, A.R., Opriessnig, T., Cossaboom, C.M., Dryman, B. A., Huang, Y.W., and Meng, X.J. (2012). Rescue of a genotype 4 human hepatitis E virus from cloned cDNA and characterization of intergenotypic chimeric viruses in cultured human liver cells and in pigs. J. Gen. Virol. *93*, 2183–2194. https://doi.org/10.1099/vir.0.043711-0.
71. Fang, W., Zhu, Y., Yang, S., Tong, X., and Ye, C. (2022). Reciprocal regulation of phosphatidylcholine synthesis and H3K36 methylation programs metabolic adaptation. Cell Rep. *39*, 110672. https://doi.org/10.1016/j.celrep.2022.110672.
72. Yang, S., Xue, J., and Ye, C. (2022). Protocol for rapid and accurate quantification of phospholipids in yeast and mammalian systems using LC-MS. STAR Protoc. *3*, 101769. https://doi.org/10.1016/j.xpro.2022.101769.
73. Sridhar, S., Situ, J., Cai, J.P., Yip, C.C.Y., Wu, S., Zhang, A.J.X., Wen, L., Chew, N.F.S., Chan, W.M., Poon, R.W.S., et al. (2021). Multimodal investigation of rat hepatitis E virus antigenicity: Implications for infection, diagnostics, and vaccine efficacy. J. Hepatol. *74*, 1315–1324. https://doi.org/10.1016/j.jhep.2020.12.028.
74. Li, T., Sakai, Y., Ami, Y., Suzaki, Y., and Isogawa, M. (2024). Strain- and Subtype-Specific Replication of Genotype 3 Hepatitis E Viruses in Mongolian Gerbils. Viruses *16*, 1605. https://doi.org/10.3390/v16101605.
75. Cao, D., Cao, Q.M., Subramaniam, S., Yugo, D.M., Heffron, C.L., Rogers, A.J., Kenney, S.P., Tian, D., Matzinger, S.R., Overend, C., et al. (2017). Pig model mimicking chronic hepatitis E virus infection in immunocompromised patients to assess immune correlates during chronicity. Proc. Natl. Acad. Sci. USA *114*, 6914–6923. https://doi.org/10.1073/pnas.1705446114.

STAR★METHODS

KEY RESOURCES TABLE

REAGENT or RESOURCE	SOURCE	IDENTIFIER
Antibodies		
Anti-GAPDH	Cell Signaling Technology	Cat# 5174; RRID: AB_10622025.
Anti-Calnexin	Cell Signaling Technology	Cat# 2679; RRID: AB_2228381
Anti-Flag	Sigma-Aldrich	Cat# F3165; RRID: AB_259529
Anti-β-Actin	Sigma-Aldrich	Cat# A5441; RRID: AB_476744
Anti-GFP	Santa Cruz Biotechnology	Cat# sc-8334; RRID: AB_641123
Anti-PLIN2 (WB)	Sangon Biotech	Cat# D261460; RRID: AB_3697350
Anti-PLIN2 (IFA)	Proteintech	Cat# 15294-1-AP; RRID: AB_2878122.
Anti-pORF3	A gift from Dr. Qiang Ding (Tsinghua University).	RRID: AB_3697352
Bacterial and virus strains		
HEV (Kernow-C1)	Dr. Suzanne U. Emerson (NIH, Bethesda, MD.	N/A
HEV (pGEM7-TW)	Dr. Xiang-Jin Meng (Virginia Tech, VA).	N/A
HEV (pSK-HEV-2)	Dr. Suzanne U. Emerson (NIH, Bethesda, MD.	N/A
BL21 (DE3)	Vazyme	Cat# C504-03
Chemicals, peptides, and recombinant proteins		
Puromycin Dihydrochloride	Yeasen	Cat# 60210ES25
DMRIE-C	Invitrogen	Cat# 10459014
mMESSAGE mMACHINE^{TM} T7	Invitrogen	Cat# AM1344
Lipidtox	Invitrogen	Cat# H34476
NVP-HSP990	Selleck	Cat# S7097
Atorvastatin Calcium	Selleck	Cat# S2077
IPTG	Sangon Biotech	Cat# A600168
HisPur^{TM} Ni-NTA Resin	Invitrogen	Cat# 88222
Polyethyleneimine (PEI)	Polysciences	Cat# 657002
Lipofectamine 3000	Invitrogen	Cat# L3000150
Deposited data		
RNA-Seq data	NCBI	GSE299317
Experimental models: Cell lines		
HEK293	ATCC	Cat# CRL-1573; RRID: CVCL_0045
HeLa	ATCC	Cat# CCL-2; RRID:CVCL_0030
Huh7-S10-3	Dr. Suzanne U. Emerson (NIH, Bethesda, MD.	N/A
S10-3-EZ	Dr. Yao-Wei Huang (South China Agricultural University)	N/A
HeLa-G1-pORF3	In this study	N/A
HeLa-G3-pORF3	In this study	N/A
HeLa-G4-pORF3	In this study	N/A
HeLa-G1-pORF3 Δ1-38	In this study	N/A
HeLa-G1-pORF3 Δ77-114	In this study	N/A
HeLa-G1-pORF3 Δ56-114	In this study	N/A
HeLa-G1-pORF3 Δ56-76	In this study	N/A
Experimental models: Organisms/strains		
C57BL/6 wild-type mice	SLAC Laboratory Animal	N/A
Gerbil	Hangzhou Medical College Experimental Animal Center	N/A

(*Continued on next page*)

Continued

REAGENT or RESOURCE	SOURCE	IDENTIFIER
Oligonucleotides		
Primers for qPCR, see Table S3	In this study	N/A
Recombinant DNA		
See Table S4 for the List of Recombinant DNA	This paper	N/A
Software and algorithms		
ImageJ	NIH	https://ImageJ.nih.gov/ij/; RRID: SCR_002285
GraphPad	Prism 9	https://www.graphpad.com/; RRID: SCR_002798

METHOD DETAILS

Mammalian cell lines and transfections

HEK293 (ATCC CRL-1573, human, female), HeLa (ATCC CCL-2, human, female), Huh7-S10-3 (Dr. Suzanne U. Emerson (National Institutes of Health [NIH], Bethesda, MD), and Huh7-S10-3-EZ cell line were generated as previously described.[30] No misidentified cell lines were used in this study among those maintained by the International Cell Line Authentication Committee (ICLAC) and NCBI BioSample databases. Cell lines were frequently checked in morphology under microscopy and tested for mycoplasma contamination but were not authenticated. To culture all cell lines, DMEM media supplemented with 10% fetal bovine serum (FBS) were employed, maintained at 37°C in an atmosphere containing 5% CO2 (v/v). For plasmid transfection, either Lipofectamine 3000 (Invitrogen, Cat# L3000150) or polyethyleneimine (PEI, Polysciences, Cat# 657002) transfection reagents were utilized. HeLa with stable expression of EGFP, pORF3s, GFP, G1-pORF3, G3-pORF3, G4-pORF3, pORF3 Δ1-38, pORF3 Δ77-114, pORF3 Δ56-114, and pORF3 Δ56-76 were obtained through transduction with a lentiviral vector, pBobi, which was selected using puromycin at a concentration of 1 μg/mL for 48 h.

Expression plasmids, reagents, and antibodies

Expression plasmid encoding HEV-G1-pORF3 was amplified from a pSK-HEV-2 HEV infection clone plasmid (GenBank accession number AF444002), Expression plasmid encoding HEV-G3-pORF3 was amplified from a Kernow-C1 p6 HEV infection clone plasmid (GenBank accession number JQ679013).[69] and HEV-G4-pORF3 was from a pGEM7-TW HEV infection clone plasmid (GenBank accession number HQ634346).[70] All the HEV infection clone plasmids are gifts from Dr. Suzanne U. Emerson (NIH, Bethesda, MD) or Dr. Xiang-Jin Meng (Virginia Tech, VA). LiveDrop-mCherry is expressed from a plasmid encoding the membrane-inserting hairpin domain (amino acids 160–216) of the glycerol-3-phosphate acyltransferase GPAT4 fused to mCherry. This fusion protein has been demonstrated to target both nascent LDs forming in the ER and mature LDs.[35] LiveDrop-mCherry is a gift from Dante Neculai (Zhejiang University). The full-length HEV (G1/G3/G4)-pORF3 and G1-pORF3 truncation constructs (Δ77-114, Δ1-38, Δ56-114, and Δ56-76) were generated by PCR-based cloning. The full-length HEV (G1/G3/G4) pORF3 and G1-pORF3 truncation constructs (Δ77-114, Δ1-38, Δ56-114, and Δ56-76) were cloned into the pBobi vector using HpaI and XbaI restriction sites, with GFP fused to the C terminus and a FLAG tag fused to the N terminus of pORF3. The DNA sequencing process was used to confirm all coding sequences.

NVP-HSP990 (Selleck, Cat# S7097) and AC (Selleck, Cat# S2077) were purchased from Selleck. Puromycin was purchased from Yesen (Yeasen, Cat# 60210ES25). Lipidtox (Invitrogen, Cat# H34476) is a Dante Neculai (Zhejiang University) gift. Mouse anti-pORF3 is a gift from Dr. Qiang Ding (Tsinghua University). Other antibodies obtained include the following: anti-FLAG (M2) (Sigma, Cat# F3165-5MG), anti-PLIN2 (BBI, Cat# D261460), anti-PLIN2 (Proteintech, Cat# 15294-1-AP), anti-β-Actin (Sigma, Cat# A5441-100UL), and anti-GFP (Santa Cruz Biotech, Cat# sc-8334).

Viruses

The stocks of the HEV infectious virus used for animal inoculation were rescued from the Kernow-C1 p6 strain.[69] The cells with persistent HEV infection were generated by transfecting Huh7-S10-3 cells with HEV-WT or HEV-null-ORF3 RNA, as previously described.[33] The G1-pORF3, G3-pORF3, G4-pORF3, or GFP fragments were inserted into the shuttle plasmid pDC315 via EcoR I and BamH I restriction sites. Recombinant adenoviral vectors expressing pORF3 variants (G1/G3/G4) with C-terminal Flag tags or GFP (Ad5-GFP) were constructed using adenoviral backbone systems. Recombinant adenoviral vectors expressing pORF3 variants (G1/G3/G4) or GFP were prepared as previously described.[59]

Quantitative RT-PCR assay

Cells receiving specified treatments or rodent tissues were lysed, and total RNA was extracted using the RNAeasy extraction kit from Axygen. cDNA synthesis was achieved using the one-step iScript cDNA synthesis kit from Vazyme. Quantitative real-time PCR was then performed using EvaGreen qPCR Master Mixes from Abm on a CFX96 real-time PCR system from Bio-Rad. Relative quantification was calculated as $2^{-\Delta Ct}$, where ΔCt represents the difference between the mean Ct value of the sample triplicates and the Ct value of endogenous L19 mRNA. The primer sequences employed in this study are detailed in Table S3.

Immunofluorescence and microscopy

HeLa or Huh7-S10-3 cells, following designated treatments, were fixed with 4% paraformaldehyde and then blocked using 2% bovine serum albumin in PBS for 1 h. Subsequently, they were incubated with primary antibodies, including anti-PLIN2, anti-Flag, anti-HEV-pORF1, anti-HEV-pORF2, and anti-HEV-pORF3, as well as Alexa-labeled secondary antibodies, with thorough washes between each step. The slides were mounted using Vectorshield and counterstained with DAPI (from Vector Laboratories). Immunofluorescence images were captured and analyzed using a Nikon Eclipse Ti inverted microscope or a Zeiss LSM880 confocal microscope.

Electron microscopy analysis

Huh7-S10-3 cells infected with Ad5-pORF3 or Ad5-GFP were fixed at 24 hpi in 2.5% glutaraldehyde (0.1 M phosphate buffer, pH 7.0), followed by 1% osmium tetroxide, and dehydrated through a graded ethanol series (30%, 50%, 70%, 80%, 90%, 95%, and 100%, 15 min each concentration). The samples were then transferred to absolute acetone for 20 min. The specimens were embedded in Spurr's resin (a ratio of acetone: 1:1 for 1 h, 1:3 for 3 h, then pure Spurr resin overnight). Ultrathin (60–80 nm) sections were double-stained with uranyl acetate and lead citrate and imaged on a Hitachi HT7700 transmission electron microscope (Hitachi High-Tech, Japan) at 80 kV with a Gatan 830 CCD camera (Gatan Inc., USA).

STED super-resolution microscopy

HeLa-pORF3 stable cells were fixed in 4% paraformaldehyde, blocked in 2% BSA/PBS, and then incubated with primary antibody (e.g., anti-PLIN2) and DyLight 521-LS NHS Ester secondary antibody (Thermo Fisher Scientific, Cat# 82495). Coverslips were mounted in Vectashield with DAPI and imaged on an STED Ultra High Resolution Microscope (Abberior Instruments GmbH, Germany).

HE and Oil Red O staining

Gerbil liver specimens were dissected and fixed in 4% paraformaldehyde at 4°C overnight. For HE staining, tissues were dehydrated using a graded ethanol series, embedded in paraffin, and sectioned at 5 μm thickness. Following standard procedures, sections were deparaffinized, rehydrated, and stained. For Oil Red O staining, liver specimens were fixed in 4% paraformaldehyde at 4°C overnight and dehydrated with isopropanol. Specimens were then immersed in Oil Red O solution for 1 h at 37°C to stain neutral lipids. After staining, specimens were rinsed with PBS to remove unbound dye. The stained liver specimens were mounted on glass slides and visualized using light microscopy. This method enabled clear visualization of LD accumulation in the liver tissue, allowing for quantification and assessment of LD localization. Relative neutral-lipid content was assessed from Oil Red O staining in two steps. First, the fraction of Oil Red O-positive pixels within the total stained field was calculated for each image [Relative area (%) = Oil Red O-positive area/total Oil Red O-stained area × 100]. Second, this value was expressed as a percentage of the control mean to enable cross-sample comparison [Normalized area (%) = sample relative area/mean relative area of controls × 100].

RNA-seq data analysis

Cells subjected to the specified treatments were harvested for RNA sequencing (RNA-Seq) analysis. Each sample was immediately lysed in 4 μL of lysis buffer containing 0.2 μL of a 1:1000 dilution of ERCC spike-in controls. cDNA synthesis was performed using the Smart-seq2 protocol, ensuring an accurate transcriptome representation. Paired-end 150 bp reads from the RNA-Seq data were aligned to the hg19 human genome reference (UCSC) using the STAR alignment tool (version 2.7.3a) with default parameters. Uniquely mapped reads were then used to quantify gene expression levels using RSEM software (version 1.3.1). Fragments per kilobase per million mapped reads (FPKM) values were calculated to estimate gene expression and normalized for both gene length and sequencing depth. Genes with an FPKM value of less than 1 across all samples were excluded from further analysis. For the remaining genes, FPKM values less than 1 were adjusted to 1 to facilitate downstream analysis. Unsupervised hierarchical clustering was performed using a correlation-based distance matrix and the hclust function in R (http://www.r-project.org). Heatmaps were generated using the pheatmap package in R. Gene set enrichment analysis (GSEA) was performed to identify pathways enriched in the differentially expressed genes.

Lipid extraction from tissue

Liver tissues from gerbils were snap-frozen in liquid nitrogen and subsequently minced into 50 mg aliquots while maintained on dry ice, and homogenized in 500 μL ice-cold methanol (LC-MS grade) containing 1.2 μL phospholipid internal standards (17:0 PC, 17:0 PE, 14:0 PS at 1.25 mg/mL) using 400 μL glass beads in screw-cap tubes with a bead-beater (5 cycles). The homogenate was centrifuged (6000 g, 2 min) through needle-punctured tubes into 1.5 mL microcentrifuge tubes, followed by bead washing with 500 μL methanol and combined flow-through collection in 15 mL glass tubes. Chloroform (2 mL) was added to the pooled supernatant, vortexed (30 s), and centrifuged (1000 g, 5 min) to separate phases. After adding 400 μL of 50 mM citric acid and 800 μL of chloroform with subsequent centrifugation (1000 g, 5 min), the organic phase was collected, aliquoted (300 μL), and vacuum-dried (20 min) for storage at −80°C.

Lipid extraction for cell and quantification by mass spectrometry

Cell lipids were extracted with chloroform/methanol (2:1) (v/v) as described previously[71,72] with some modifications. Cells were quenched using 1 mL mass spectrometry-grade methanol pre-cooled at −40°C after a brief wash with pre-warmed PBS, then lysed with 5 freeze-and-thaw cycles. The lysates were then transferred to glass tubes, and 2 mL of chloroform was added and vortexed for lipid extraction. After centrifugation, the supernatants were transferred to glass tubes. An additional 800 μL of chloroform and 400 μL of 50 mM citric acid were added to achieve phase separation. The lipid phase was equally taken and dried by a vacuum concentrator system (Labconco). A triple quadrupole mass spectrometer (the QTRAP 6500 + System) was used for lipid quantitative analysis per an established protocol.[72]

To quantify neutral lipids such as TAG and sterol ester, a mixture of methanol and dichloromethane (1:1, v/v) containing 5 mM ammonium acetate and Lipidomix was used to dissolve lipid extracts. Lipids separated chromatographically on a C18 column (ACQUITY UPLC BEH C18 column, 130A, 1.7 μm, 2.1 mm × 50 mm) were followed by quantification using multiple reaction monitoring (MRM) transitions of mass spectrometry. Specifically, liquid chromatography was programmed as follows: Buffer A contains 33.3% methanol, 33.3% acetonitrile, 33.4% water, 5 mM ammonium acetate, and Buffer B contains 5 mM ammonium acetate in 100% isopropanol. The retention time for each MRM peak was compared to an appropriate standard. The area under each peak was quantified using Analyst software and re-inspected for accuracy. For each lipidomics dataset, only lipids exhibiting a >1.5-fold difference from control at $p < 0.05$ (unpaired two-tailed t test) were visualised. The resulting heatmap displays, per cell line or liver sample, the twenty most abundant triacylglycerol (TAG) species plus all four detected cholesteryl-ester (CE) species, ordered by signal intensity. Targeted lipid mass spectrometry raw data is available in Table S2.

Recombinant protein expression and purification

Recombinant G1-pORF3 fused to GFP to its C terminus was produced in *E. coli* BL21(DE3) cells following induction with 0.5 mM IPTG for 4 h at 37°C (220 rpm). Bacterial pellets were sonicated in Ni^{2+}-binding buffer (20 mM HEPES, 1 M NaCl, 1 M urea, pH 7.4) supplemented with a protease-inhibitor cocktail and 1 mM PMSF. The His-tagged protein was captured on Ni-NTA resin, washed, and eluted with 500 mM imidazole in the same buffer. Final polishing by size-exclusion chromatography (Superdex 75 10/300 GL) in gel-filtration buffer (20 mM HEPES, 500 mM NaCl, pH 7.4) yielded homogeneous G1-pORF3-GFP suitable for downstream assays.

High-fat diet and cholesterol regulation

Gerbils (purchased from Hangzhou Medical College Experimental Animal Center) were maintained in appropriate animal biosafety level 2 (ABSL-2) laboratories at Zhejiang University Experimental Animal Center. All animal experiments were conducted strictly following guidelines approved by the Animal Ethics Committee of Zhejiang University (ZJU20181049). Briefly, 30 SPF gerbils (male, 8 weeks old) were divided into five groups: vehicle group (6 gerbils), high-fat diet group (6 gerbils), HEV infection group (6 gerbils), HEV+high-fat diet group (6 gerbils), and HEV+ AC group (6 gerbils) with AC treatment (60 mg/kg/day, divided into three doses daily). In all 3 HEV infection groups, gerbils were each inoculated intraperitoneally with 1 mL of the infectious virus stock containing approximately 1.67×10^6 GE/mL. The HEV infection model in gerbils was developed as described previously.[60,73,74] All gerbils were sacrificed at 14 dpi, and sera were collected to measure TAG, TCHOL, HDL, and LDL levels. Liver and feces samples were analyzed for HEV RNA titers by real-time RT-PCR.[75] Histopathologic evaluations were performed on liver sections using HE and Oil Red O staining.

Gerbil infection of HEV WT and HEV-null-ORF3

18 SPF gerbils (male, 8 weeks old) were randomly allocated into three groups: a vehicle control group (6 gerbils), a HEV infection group (6 gerbils), and a HEV-null-ORF3 infection group (6 gerbils). In wild-type HEV and HEV-null-ORF3 infection groups, gerbils were each inoculated intraperitoneally with 1 mL of the infectious virus stock (HEV or HEV-null-ORF3) containing approximately 1.67×10^6 GE/mL, respectively. At 14 days post-infection (dpi), all gerbils were sacrificed, and sera were collected to determine TAG, TCHOL, HDL, and LDL levels. Additionally, real-time RT-PCR was used to assay liver and feces samples for HEV RNA titers. Histopathological assessments were then conducted on liver sections using HE and Oil Red O staining.

Adenovirus infection in gerbils

For recombinant adenovirus infection, a system expressing EGFP and G1-pORF3 in gerbil liver was designed and produced according to previously described methods. Gerbils (male, 8 weeks old) were randomly assigned to groups and intraperitoneally inoculated with 1 mL of recombinant adenovirus stock containing approximately 5×10^8 TCID[50] on day 0 ($n = 6$/group). Sera were collected from gerbils 14 dpi to determine TAG, TCHOL, HDL, and LDL. Subsequently, gerbils were euthanized, and histopathological analyses were performed on liver sections using H&E staining and Oil red staining, as indicated.

QUANTIFICATION AND STATISTICAL ANALYSIS

Statistics and reproducibility

Quantitative data are presented as mean ± standard error of the mean (SEM) derived from at least three independent experiments. Where appropriate, statistically significant differences between multiple comparisons were determined using the one-way ANOVA test with Bonferroni correction. Significance was set at $p < 0.05$. Only properly preserved and processed samples were included in the analyses; no samples or animals were excluded. Statistical methods did not determine the sample size, and randomization was not used in experiments except those involving animals. To ensure reproducibility, all experiments, except compound screening, were independently replicated at least three times with consistent results. Investigators were not blinded to allocation or outcome assessment during the experiments, except for assessing the Ishak score for HEV-induced liver injury.

LD quantification

LD metrics, including fluorescence intensity, number per field, and diameter, were extracted from single confocal z-slices rather than whole-cell volumes. After staining, the LD channel was converted to 8-bit in ImageJ, inverted, and thresholded to isolate LD signals. Using Analyze → Set Measurements, we recorded integrated density and area, calculated mean fluorescence intensity (integrated density/area), and expressed it relative to controls. LD abundance was scored as the number of droplets per field of view, counted manually on the same z-slice. The scale bar was calibrated for size analysis, the image thresholded, and a line was drawn across each LD to measure its diameter; values were then normalised to the control mean.

ADDITIONAL RESOURCES

This study did not involve any clinical trials.